UNIVERSIDAD DE CHILE
FACULTAD DE CIENCIAS FÍSICAS Y MATEMÁTICAS
DEPARTAMENTO DE FÍSICA

INDUCING A TOPOLOGICAL TRANSITION IN GRAPHENE NANORIBBONS
SUPERLATTICES BY EXTERNAL STRAIN

TESIS PARA OPTAR AL GRADO DE
MAGÍSTER EN CIENCIAS, MENCIÓN FÍSICA

ESTEBAN ANDRÉS FLORES GUTIÉRREZ

PROFESOR GUÍA:
FRANCISCO JAVIER MUÑOZ SÁEZ

MIEMBROS DE LA COMISIÓN:
EDUARDO BRINGA
CAROLINA PARRA GONZALEZ

SANTIAGO DE CHILE
2022

Resumen

Inducción de una transición topológica en superredes de nanocintas de grafeno por esfuerzo externo

Esta tesis tiene como propósito estudiar la existencia de estados localizados en superredes, que pueden ser utilizados en dispositivos nanoelectrónicos.

Estas ideas nacen con la observación de estados localizados en el poliacetileno, lo que generó un ejemplo simple de aisladores topológicos: materiales aislantes que, bajo ciertas condiciones, presentan estados localizados de baja energía en sus bordes, siendo aislantes en su bulto. Este modelo fue propuesto por Su, Schrieffer y Heeger (SSH).

Por otro lado, un material que tiene un conjunto de simetrías similares al poliacetileno es el grafeno. Un material bidimensional en el que los átomos de carbono están dispuestos en una red hexagonal o de panal de abejas. Además, el Premio Nobel de 2010 fue otorgado a Geim y Novoselov por sintetizar este material.

Esta tesis se centra en las consecuencias electrónicas y mecánicas de unir diferentes segmentos de nanocintas de grafeno (GNR). En ciertos casos, los segmentos GNR forman una superred que reproduce el modelo SSH a energías cercanas al nivel de Fermi. Encontramos un mecanismo general para controlar los patrones de enlace similares al SSH con esfuerzo externo, incluso se puede inducir una transición topológica a valores moderados de esfuerzo.[1] En particular, para una combinación específica de GNR, encontramos una transición topológica entre $\approx 3 - 5\%$ de esfuerzo. Los estados similares a SSH son sorprendentemente robustos, incluso cerca de la fractura del material.

Abstract

The purpose of this thesis is to study the existence of localized states in superlattices, which can be used to create nanoelectronic devices.

These ideas are born with the observation of localized states in polyacetylene, which provided a simple example of topological insulators: insulating materials that, under certain conditions, present low energy localized states at their edges, meanwhile being insulating in the bulk. This model was proposed by Su, Schrieffer and Heeger (SSH).

On the other hand, a material that has a set of symmetries similar to polyacetylene is graphene. A two-dimensional material in which carbon atoms are arranged in a hexagonal or honeycomb lattice. Furthermore, the 2010 Nobel Prize was awarded to Geim and Novoselov for synthesizing this material.

This thesis focus on the electronic and mechanical consequences of joining different segments of graphene nanoribbons (GNR). In certain cases the GNR segments form a superlattice reproducing the SSH model at energies close to the Fermi level. We found a general mechanism to control the SSH-like bonding patterns with external strain, even a topological transition can be induced at moderated strain values.[1] In particular, for a specific combination of GNRs, we found a topological transition between $\approx 3 - 5\%$ of strain. The SSH-like states are surprisingly robust, even close to the fracture of the material.

To my family

Acknowledgments

Table of content

List of Figures

Chapter 1

Introduction

Since its exfoliation, graphene has been an object of intense research by its exotic electronic properties, which are interesting for both, basic and applied science[3, 4, 5, 6, 7, 8, 9, 10, 11]. Nevertheless, the lack of a bandgap has hindered its utility in electronic devices and the realization of exotic topological states. Different approaches, experimental and theoretical, to generate gapped graphene are developed, such as graphene bilayer with a gate voltage [8, 12] or applying uniaxial strain has been proposed., [13, 14] as well as topological currents[15, 16, 17]. Even more exotic topological effects are predicted to appear in the twisted bilayer graphene[18, 19].

Strips of graphene, or graphene nanoribbons (GNRs) can be either insulating or metallic according to their chirality[20]. A particular family of them, the armchair GNRs – denoted as N-AGNRs [21, 22, 23, 24, 25, 26], with N as the number of C atoms along the width of the ribbon – are metallic if they satisfy $N = 3p + 2$ (where p is an integer), otherwise they are semiconducting. The traditional "top-down" synthesis methods of GNRs (e-beam lithography [27], nanowire lithography [28], *etc.*) as well as some "bottom-up" methods (unzipping of carbon nanotubes [29], epitaxial growth epitaxial growth [30], *etc.*) offer little control over chirality and uniformity. Nevertheless, the recent development of a bottom-up approach to synthesize GNRs from precursor molecules has allowed precise control of the chirality and width of the GNRs [31]. The last method has been successfully applied to build more complex systems [32], such as GNRs with a specific periodic modulation in their width [33]. Recently, two works by Grönig *et al.*[2] and Rizzo *et al.*[34] demonstrated that periodic superlattices of N-AGNR/M-AGNR (different width) host topologically protected edge states, in close analogy with the Su-Schieffer-Heeger (SSH) model of polyacetylene[35]. Indeed, there is a width dependence in the topological classification of N-AGNR, where topological states appear at the boundary between two insulating AGNRs with different topological phases[36, 37, 38, 39]. An engaging system that meets with this condition is the 7-AGNR/9-AGNR interface[2, 34].

If two of such N/M-AGNR junctions are close enough, their localized states will hybridize with each other (*i.e.* an artificial dimer molecule). Additionally, if these boundary states are periodically repeated, they form a superlattice energy band. By controlling the spatial sequence and the distance between the junctions, it is possible to have two different interaction

strengths between different topology-derived localized states. In this way, the SSH model can be emulated in the low-energy description of modulated AGNRs. The SSH model has two different topological phases, and they translate – by the bulk-boundary correspondence principle – in the existence/absence of zero-energy, localized edge states at the end of the sample [40, 41]. In the case of a superlattice, these edge states will appear at the superlattice's edges [42].

The last ingredient for our work is strain. While in graphene uniaxial strains as large as 30% do not split the Dirac cone [43, 14] it is well known that a moderate strain can increase or decrease the band gap of an N-AGNR, depending whether $N = 3p$ or $N = 3p + 1$ [44]. However, strain cannot induce any topological transition in GNRs [45]. In this work we will show that strain can be exploited to induce a topological transition in AGNR superlattices, effectively switching the SSH-like bands from trivial to topological or vice versa. It is worth noting that, so far, there are only a few proposals to induce a controllable topological transition in GNRs [46, 47].

This thesis is based in a large number of well-established results in condensed-matter physics. A major part of my thesis work was to understand them and learn how to establish relationships among these concepts and results. Then, a large fraction of this thesis is dedicated to explain them in detail. This start by introduction the SSH model of polyacetylene in Section 2, this model establish the simplest model of a topologically non-trivial system, and important concepts such as the *bulk-boundary correspondence*. Then, in Section 3, we will elaborate on graphene and graphene-like systems, particular attention will be given to the AGNRs. In Section 4 we will establish the emergence of topologically-protected states at the interface between two AGNRs of different width, and generalized for a superlattice at Section 5. At this point we study the response of these superlattices to uniaxial strain, first from an entirely mechanical point of view, see Section 5.1, and then from its consequences on the electronic structure, and the emergence of topologically-protected states, see Section 5.2. The emergence of the topologically-derived edge states as a function on the strain is far from an abrupt process, and to understand them we defined a global index, based on a local property of a SSH-like state: the sublattice polarization, explained in detail in Section 5.3. The methods employed along this thesis are detailed in Section 5.4. Finally, a summary of this thesis is provided in section 6.

Chapter 2

Su-Schrieffer-Heeger (SSH)

2.1 Tight binding model

The model proposed by Su-Schrieffer-Heeger (SSH) to detail the conduction properties of polyacetylene has been widely used in condensed matter and has undoubtedly established itself as the model par excellence to explain topological insulators [35]. The following discussion will be based mainly on Refs. [41, 48].

Polyacetylene is an organic molecule composed of carbon and hydrogen atoms. It is characterized by alternating single and double bonds. In this way the carbon fulfills the octet rule and stabilizes. Polyacetylene chemical formula is $(CH)_{2N}$. In this formulation, the spinless electrons are in a one-dimensional lattice. These assumptions showed the existence of edge states, called solitons, which would be the basis for explaining the electronic behavior of polyacetylene [35].

To analyze this behavior, the Hückel method (basically a type of *tight-binding* model) will be used. This formalism can be applied to hydrocarbon molecules and ignores the σ bonds, considering exclusively the π bonds, perpendicular to the chain plane, that is, the p_z orbitals, *i.e.* a single orbital is considered per hydrocarbon [49].

The interaction energy is expressed through the components of the Hamiltonian:

$$\langle \psi_i | H | \psi_j \rangle = \left\{ \begin{array}{lll} \alpha & \text{if} & i = j \\ \beta & \text{if} & i \neq j, \end{array} \right. \tag{2.1}$$

with α the on-site energy and β the interaction energy between different sites. For our purposes it is enough to consider an interaction to first neighbors, ignoring more distant neighbors because their interaction energy is negligible, so that, in the second case only the elements $j = i \pm 1$ are non-zero.

The parameter α can be set to zero if all atoms are equal, and have the same environment, as is the case with polyacetylene.

As stated above, in polyacetylene, the single and double bonds are alternating along the chain, so the energy of interaction between the orbitals varies following the previous pattern.
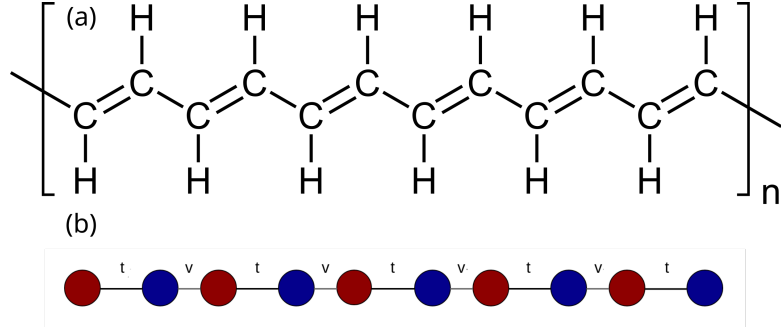
Figure 2.1: (a) Kekulé structure of polyacetilene. There exist carbon atoms in the main chain and each of them have an hydrogen atom. (b) The alternance of single and double bond is represented by a different sites and different neighbour interaction energy in the tight-binding model. Since the atoms are the same, the site energy is zero.

For certain carbon atoms the double bond will be to their right and for others it will be to their left. Therefore, we will have to consider two carbon atoms per unit cell that we will call a_i and b_i (i is the index of the unit cell). The orbitals associated with the valence electrons will be written as $\psi_{i,a}$ and $\psi_{i,b}$. Thus, the interactions between neighboring carbons (*e.g.* β) are written as follows:

$$t = \langle \psi_{i,a}|H|\psi_{i,b}\rangle \tag{2.2}$$

$$v = \langle \psi_{i,b}|H|\psi_{i+1,a}\rangle, \tag{2.3}$$

the double bond or intracell coupling is t, while v is the single bond or intercell coupling. It is because of the existence two nonequivalent carbon atoms, that posses two different interaction energies in the Hamiltonian. This Hamiltonian written in the base of the atoms -ordered form the left to the right (see Figure 2.1)- is represented in a matrix as follows:

$$H = \begin{pmatrix} 0 & t & 0 & 0 & 0 & \cdots \\ t & 0 & v & 0 & 0 & \cdots \\ 0 & v & 0 & t & 0 & \cdots \\ 0 & 0 & t & 0 & 0 & \cdots \\ \vdots & \vdots & \vdots & \vdots & \vdots & \ddots \end{pmatrix} \tag{2.4}$$

It can be noted that the terms of the diagonal correspond to the site energy set to zero for convenience, because it has been established that all the atoms correspond to carbon atoms with the same energy. This Hamiltonian is Hermitian. Finally, it is important to emphasize that free boundary conditions have been used in this system.

This Hamiltonian can be represented through the second quantization formalism as [48]:

$$H_{SSH} = t\sum_{j=0}^{N} a_j^\dagger b_j + v\sum_{j=0}^{N-1} a_{j+1}^\dagger b_j + H.c., \tag{2.5}$$

2.2 Edge states

The energy of each state is obtained by diagonalizing the Hamiltonian shown in Equation 2.4. From this procedure, three qualitatively different set of solutions are obtained for the system, depending on the values of the intracell and intercell interactions (t and v). The trivial case is obtained when the intracell interaction energy is larger than the intercell interaction, that is, $t > v$, as seen in Figure 2.2 *(a)* [48]. In this situation, delocalized states are observed for highest occupied molecular orbital (HOMO) and lower unoccupied molecular orbital (LUMO), although this occurs for all states of the system. In addition, there is an energetic "band-gap" between HOMO and LUMO, which, in the case of having a infinitely long chain, is given by $2|t - v|$ [42].

On the other hand, if both, the intercell and intracell interaction energies are close, so that $t \approx v$, the chain starts to have a metallic behavior, which can be identified with the closure of the band-gap energy.

Finally, the case in which $v > t$ is obtained (Figure 2.2 *(b)*). For all bands with non-zero energy, this case is nearly identical to the trivial case, *i.e.* it has an energetic band-gap. However, there is a pair of nearly zero-energy bands, whose wavefunctions are localized at the edges of the chain. The wavefunctions of these edge states (labelled ψ_L if it is localized at the left edge and ψ_R if it is localized at the right side of the chain) can be written as:

$$\psi_L^\dagger = \alpha \sum_{j=0}^{N-1} (-1)^j \exp\left(-\frac{j}{\varepsilon}\right) a_j^\dagger, \tag{2.6}$$

$$\psi_R^\dagger = \beta \sum_{j=0}^{N-1} (-1)^j \exp\left(\frac{N-j}{\varepsilon}\right) b_j^\dagger, \tag{2.7}$$

with α, β normalization constants, $\varepsilon = \log\left(\frac{v}{t}\right)$. If the chain is short enough, these states have a non-zero overlap, and interact forming a bonding and anti-bonding pair, with a interaction energy $\langle|\psi_L|H|\psi_R\rangle \propto e^{-N/\varepsilon}$, as seen in Figure 2.2 *(c)*[42], with and N the number of unit cells that exist in the system, remember that the number of sites (atoms) is $2N$.

To quantify the degree of localization of a state, we used the Inverse Participation Ratio (IPR):

$$IPR = \frac{\left(\sum_i ||\psi_i||^2\right)^2}{\left(\sum_i ||\psi_i||^4\right)}, \tag{2.8}$$

when this index is equal to 1, the state is completely localized, but if the wave function is uniformly distributed over the system, that is, fully delocalized, the IPR will have its maximum value, which is the number of sites($IPR = N$). Figure 2.2 *(d)* shows the transition of the bands as the intercell parameter varies, noting the appearance of localized states close to zero energy when this interaction is greater than the intercell.
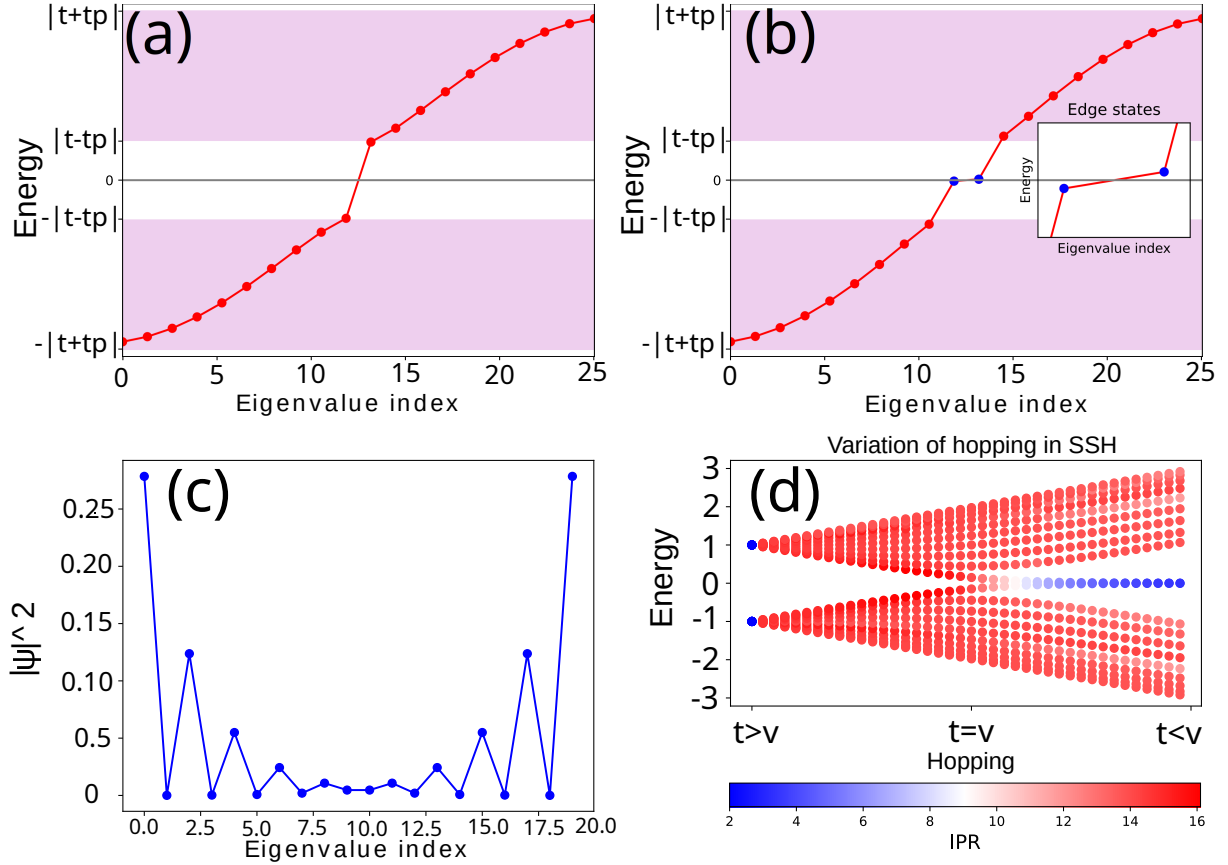
Figure 2.2: (a) Energy in the reciprocal space of a finite SSH-system with intracell energy greater than intercell energy $t > v$. (b) Energy in the reciprocal space of a finite SSH-system with intercell energy greater than intracell energy $t < v$. In this situation appear two states with a residual energy close to zero (see the inset). (c) Eigenfunction with energy close to zero. (d) Energy values varying the interaction energy t while keeping v fixed. States close to zero energy appears when $t < v$.

2.3 Chiral Symmetry

To understand the existence of zero-energy edge states, it is necessary to remember that the system is made up of a bipartite lattice of equal but non-equivalent atoms due to the bond alternation. This generates an additional symmetry in the SSH-chain called *chiral* symmetry.

To understand this symmetry, it is practical to change the order of the basis of the Hamiltonian (Equation 2.4) to put it in block diagonal form. This can be done because the permutations do not affect the properties of the system [48], so that:

$$H = \begin{pmatrix} 0 & H_{ab} \\ H_{ab}^T & 0 \end{pmatrix}, \tag{2.9}$$

since there are no interactions among next-nearest neighbors, $H_{aa} = H_{bb} = 0$. Now, the chiral operator Γ is defined as:

$$\Gamma = \begin{pmatrix} I_n & 0 \\ 0 & -I_n \end{pmatrix}, \tag{2.10}$$

with I the identity matrix $N \times N$. We note that it has a similar shape to the Pauli matrix σ_z.

It is easy to see that chiral operator anti-commutes with the Hamiltonian:

$$H\Gamma - \Gamma H = 0 = \{H, \Gamma\} \tag{2.11}$$

This chiral symmetry is directly related to the existence of two nonequivalent sites in the system, which is why it is also called *sublattice symmetry*. From the chiral operator, it is possible to define the orthogonal projection operators on each site of the sublattice:

$$P_a = \frac{1}{2}\left(I + \Gamma\right), \qquad\qquad P_b = \frac{1}{2}\left(I - \Gamma\right) \tag{2.12}$$
$$\implies P_a H P_a = P_b H P_b = 0; \qquad H = P_a H P_b + P_b H P_a \tag{2.13}$$

This generates implications in the energy spectrum. The eigenvalues of the system must come in pairs. If ψ is a solution of the system with energy E, then $\Gamma\psi$ is the eigenstate of the system with energy $-E$. These eigenstates are called chiral pairs and both have equal support (non-zero coefficients) in both sites of the sublattice [48].

In the case of a state with zero energy, we have that $E = -E = 0$, therefore, this state is its own chiral pair. This implies that this state, let's say the one on the right (at site a), is only supported by a sites. In the same way it happens with the site located b at the other end of the chain, see Figure 2.2 c.

Finally, it is important to mention that edge states are robust to disorder, due to the chiral symmetry protection [42]. In a general extended state ψ_E ($E \neq 0$), if we change t, v by means of disorder (at each site), the state's energy and wave function will be modified, but due to the chiral symmetry the state ψ_{-E} will need to change accordingly. This can not be the case for a edge state with energy $E = 0$, let assume we only add disorder to the left edge of the system, and the state ψ_L changes its energy to δE (any non-zero value). Then its chiral partner, the edge state at the right ψ_R, must change its energy to $-\delta E$. But there is no disorder nor interaction with ψ_L to induce such changes, hence the energies of the edges states must be zero, regardless of the disorder. The previous analysis is valid as long as the chiral symmetry is present (Equation 2.11).

A simple way to break the chiral symmetry, and hence the robustness of zero-energy states against disorder is by means of adding a non-uniform on-site energy to the Hamiltonian (*i.e.*, adding non-zero at the diagonal of Equation 2.4).

2.4 Bulk

So far the discussion has focused mainly on the edges of the chain, but has not gone into depth on bulk. We will see that both are closely related.

For this, we have to contextualize the limit cases for the ssh chain where they are fully dimerized. One of these is when the interaction between cells is removed, *i.e.* $v = 0$. The dimers are isolated from each other. In the cases where the $t > v$ condition is maintained, it will be said that the same topological phase will be maintained.

The next case where we have a fully dimerized chain is when we have a finite intercell energy, but the intracell interaction energy has been cancelled. In this situation, the first site will be isolated (non-interacting) and the last site will be in the same condition. Again completely isolated dimers exist along the bulk, but both non-bonding atoms at the edges have zero-energy. In this context, as long as the $v > t$ condition holds, the systems will have the same topological phase.

Thus, a third and final topological phase is mentioned connecting both cases, the metallic case, when $t = v$.

Before continuing, it is necessary to specify what is meant by topology. From mathematics, it is an area that studies the properties of a body modified by continuous transformations. For insctance it is stated that a ring and a coffee cup are topologically equivalent, because they have a single hole or one genus. However, when comparing these elements with a ball, it is concluded that they are topologically nonequivalent, because the sphere does not have holes or his genus is zero. In what brings us together in this thesis, the continuous transformations will be carried out on the intercell and intracell interactions.

That stated in the last paragraphs can be expressed through the Hamiltonian described in the previous subsections, but this time taking some considerations into account. First, periodic boundary conditions will be used. In addition, in this case an infinite system will be used, because the aim is not to study the edges, but rather the behavior of the bulk. This will allow us to use Blöch's theorem, since there is translation symmetry and there are no defects in the chain. With this, the Fourier transform is used and the situation is taken to the reciprocal space of momentum. In this way the Hamiltonian, in the momentum space is:

$$H = \begin{pmatrix} 0 & v + we^{-ik} \\ v + we^{ik} & 0 \end{pmatrix} \tag{2.14}$$

It is just a 2×2 matrix, which for simplicity can be written in terms of the Pauli matrices:

$$H = d_x \sigma_x + d_y \sigma_y + d_z \sigma_z, \tag{2.15}$$

with $\vec{d}(k) = (d_x(k), d_y(k), d_z(k)) = (t + v \cos(k), v \sin(k), 0)$ and σ_i the Pauli matrices. The energies of the system are obtained by diagonalizing the Hamiltonian, obtaining the following expression:

$$E = \pm\sqrt{t^2 + v^2 + tve^{ik} + tve^{-ik}} = \pm\sqrt{t^2 + v^2 + 2tv \cos(k)} \tag{2.16}$$

The width of the band-gap in the energy bands is $2|t - v|$ and is obtained using the value of $k = \pi$ in the equation above.

The relation that is made from the SSH model explained with the topology, is obtained through the Hamiltonian, in particular with the function d that multiplies the Pauli matrices.
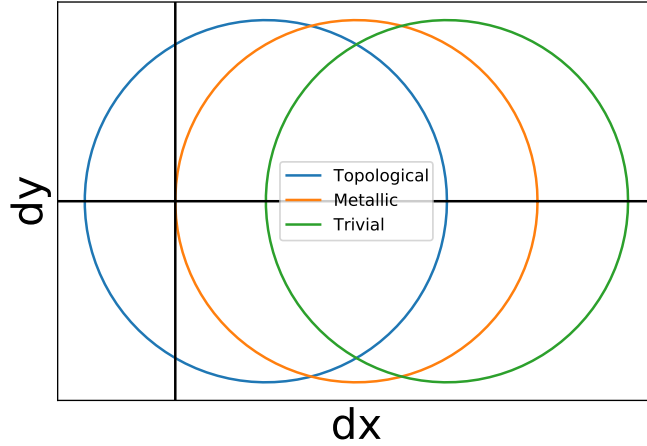
Figure 2.3: Function $d(\vec{k}) = (t + v\cos(k), v\sin(k), 0)$ representing a circle in reciprocal space. From this curve the SSH winding number is defined. If this curve encloses the origin once, then its topological number is one $v > t$, this is the case of a topological insulator. If the curve does not encloses the origin, the winding number is zero, being a trivial insulator $t > v$. There is a metallic case when the circle passes through the origin $t = v$, and the winding number is undefined.

This function defines a circumference of radius v that is translated t units from the origin, on the horizontal axis. From this, the winding number ν is defined.

If the circle does not enclose the origin, then $\nu = 0$, this occurs when $t > v$ and this case is called a trivial insulator. By increasing the value of the intercell interaction, we reach the situation in which $t = v$, we have an undefined winding number and we have a metallic case. Finally, continuing the increase of this interaction between sublattices with $t < v$, we have that the circumference encloses the origin and in this case $\nu = 1$, obtaining a topological insulator.

In general, the winding number will not change as long as the conditions of $t > v$ or $t < v$ hold. This number will be undefined, as already mentioned, in the metallic case or when the chiral symmetry of the system is broken. To break the chiral symmetry there must be a non-zero term multiplying the Pauli matrix σ_z, which represents precisely the chiral symmetry operator seen in the previous section. In this case, the circumference defined by the function d leaves the plane xy, therefore the number of the winding cannot be defined.

In general, the winding number can be determined for a band that is fully occupied. In the one-dimensional context it is called the Zak phase [50] and is obtained through the formula:

$$\nu = \frac{1}{2\pi} \oint \frac{1}{|d|} \left(d(k) \times \frac{d}{dk} d(k) \right)_z dk \qquad (2.17)$$

Finally, it has been proved that when the topological number is different from zero, there are localized states of energy close to zero. In the literature, this feature is called the bulk-

boundary correspondence.[48]

2.5 Bipartite lattice of domain walls states

The SSH model described in the previous sections is essential to control the electronic properties in superlattices. In this subsection, localized zero-energy states will be used to recreate the Hamiltonian obtained for the SSH model. This section will be based on Ref. [42].

One way to get localized states is through a domain wall defect c[35]. This type of defect is generated when the alternation between intercell-intracell interactions is interrupted and reversed. This mechanims consist on the following, lets consider a SSH chain with bonds $t - v - t - v$ (and so on). But, somewhere this alternation breaks, where there should be a bond v, it is exchanged for a bond t. Another way to understand this is that a SSH chain with trivial topology and N sites is concatenated with one with non-trivial topology with N sites and, in addition, periodic boundary conditions are included (Figure 2.4).
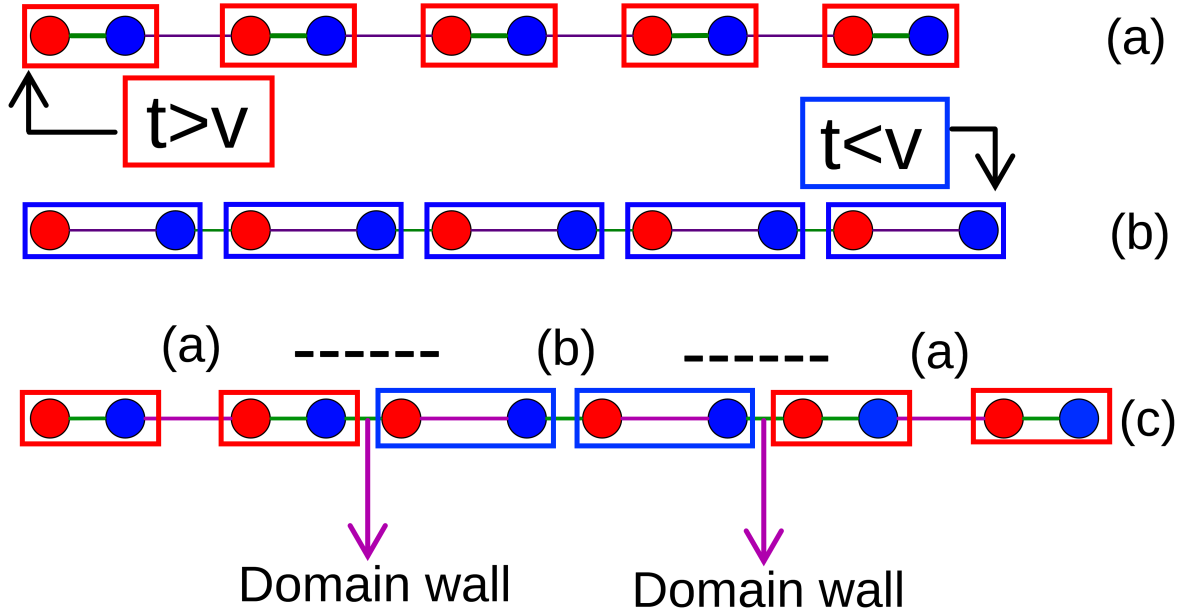
Figure 2.4: (a) scheme of the structure of an SSH chain with trivial topology, the case when the intracell coupling is greater than the intercell coupling. (b) represents the opposite case. Finally, in (c) the union of chains of different topology can be seen forming a domain wall defect, forming a chain with this type of this defect.

Thus, the Hamiltonian for this new superlattice can be written as:

$$H_{DW} = \sum_{j=0}^{N-1} \left(t a_j^\dagger b_j + v a_{j+1}^\dagger b_j \right) + \sum_{j=N}^{2N-1} \left(v a_j^\dagger b_j + t a_{j+1}^\dagger b_j \right) + H.C \qquad (2.18)$$

10

diagonalizing this system will show two localized states corresponding to the sites where these domain walls exist, see Figure 2.5. While the domain wall states are determined using the edge state equations from the previous sections:

$$\psi_a^\dagger = \alpha \sum_{j=0}^{N-1} (-1)^j \exp\left(-\frac{j}{\varepsilon}\right) a_j^\dagger + \alpha \sum_{j=N}^{2N-1} (-1)^j \exp\left(-\frac{2N-j}{\varepsilon}\right) a_j^\dagger, \tag{2.19}$$

$$\psi_b^\dagger = \beta \sum_{j=0}^{N-1} (-1)^j \exp\left(\frac{N-j-1}{\varepsilon}\right) b_j^\dagger + \beta \sum_{j=0}^{N-1} (-1)^j \exp\left(\frac{j-N}{\varepsilon}\right) b_j^\dagger, \tag{2.20}$$

As can be seen in Figure 2.5, the states are located in the middle of the chain and at the beginning-end (remember the imposed periodic boundary conditions).

These states depend on the length of each subchain, as the above equations show. So the idea now is to hybridize these localized states so that they interact with an overlapping energy. In this way, the system can be dimerized, so that there are two interaction energies that depend on the length of each chain and the intercell and intracell energies can be redefined only by controlling the length of the trivial and topological chain.

To do this, Munoz $et\ al.$[42] constructed a Hamiltonian in which these strings are periodically repeated, so that they interact with finite energy:

$$H_{BDW} = \sum_{m=0}^{M} h_N(m) + h'_{N'}(m), \tag{2.21}$$

with:

$$h_N(m) = \sum_{j=2mN}^{(2m+1)N-1} \left(ta_j^\dagger b_j + va_{j+1}^\dagger b_j\right) + H.C \tag{2.22}$$

$$h'_{N'}(m) = \sum_{j=(2m+1)N'}^{(2m+2)N'} \left(va_j^\dagger b_j + ta_{j+1}^\dagger b_j\right) + H.C \tag{2.23}$$

By varying the size of the trivial and topological chains, different results were obtained. Having one chain longer than the other, a small band can be seen within the fundamental gap of the spectrum (Figure 2.7 b). Within these bands there is an inner gap with localized states at the edges and are formed by the domain wall states. Like the states of the original SSH model, they are also polarized, but this time on each sublattice segment. On the other hand, in the spectrum of the system formed by chains of the same length (Figure 2.7 (a)), a gapless, isolated band arises in the middle of the fundamental band gap.

In this way, an effective Hamiltonian for the SSH supelattice, similar to the original Hamiltonian is constructed:
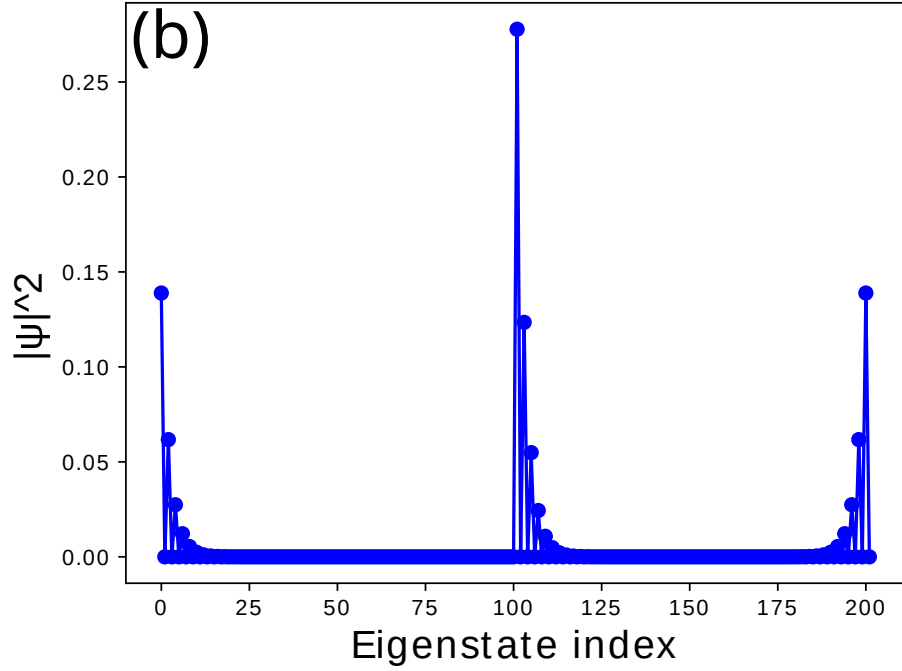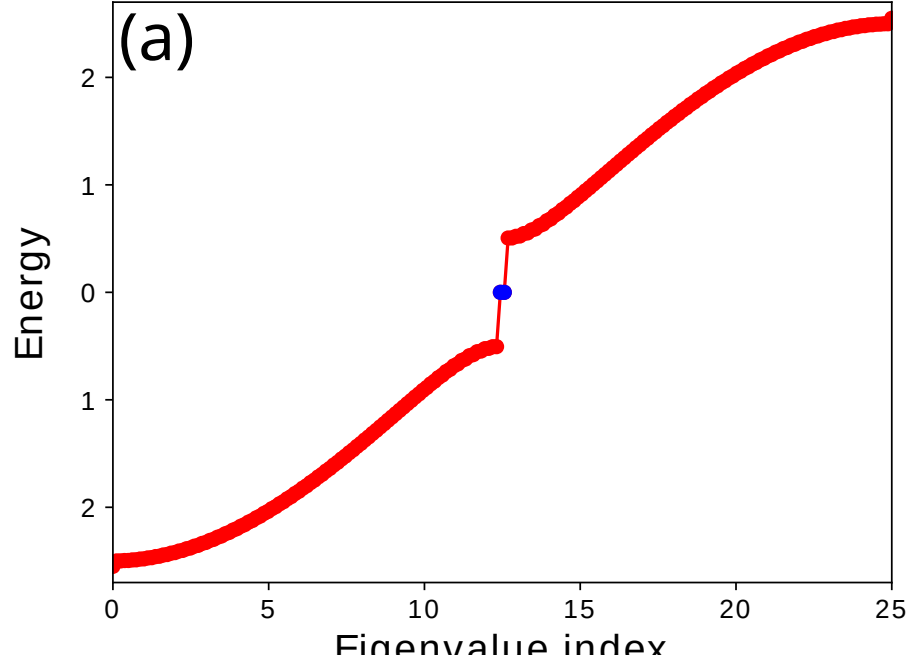
Figure 2.5: (a) eigenenergies for the union of two chains of different topology. Close to zero energy, a state associated with the domain wall appears. (b) Eigenmode of the domain wall defect. Periodic boundary conditions (PBC) have been considered.

$$H_{BDW}^{Eff} = \sum_{m=0}^{M-1} t'(\psi_{a,m}^{\dagger}\psi_{b,m}^{\dagger}) + v'(\psi_{a,m+1}^{\dagger}\psi_{b,m}^{\dagger}) + H.C. \qquad (2.24)$$

12

with:

$$t' = \langle \psi_{a,k} | H_{DW} | \psi_{b,k} \rangle \propto N \exp\left(-\frac{N}{\varepsilon}\right)\left(t \exp\left(\frac{1}{2\varepsilon}\right) - v \exp\left(-\frac{1}{2\varepsilon}\right)\right) \qquad (2.25)$$

$$v' = \langle \psi_{a,k+1} | H_{DW} | \psi_{b,k} \rangle \propto N' \exp\left(-\frac{N'}{\varepsilon}\right)\left(t \exp\left(\frac{1}{2\varepsilon}\right) - v \exp\left(-\frac{1}{2\varepsilon}\right)\right). \qquad (2.26)$$

In this way, the Hamiltonian of the SSH has been reconstructed with a superlattice. But this time with a spatial difference, with a greater number of sites per network and also with a different energy scale. In addition, they have shown that these states are robust to the breaking of chiral symmetry and, therefore, to disorder, both at the site and between cells. All properties can be verified in the work done by Mella *et.al* [42].
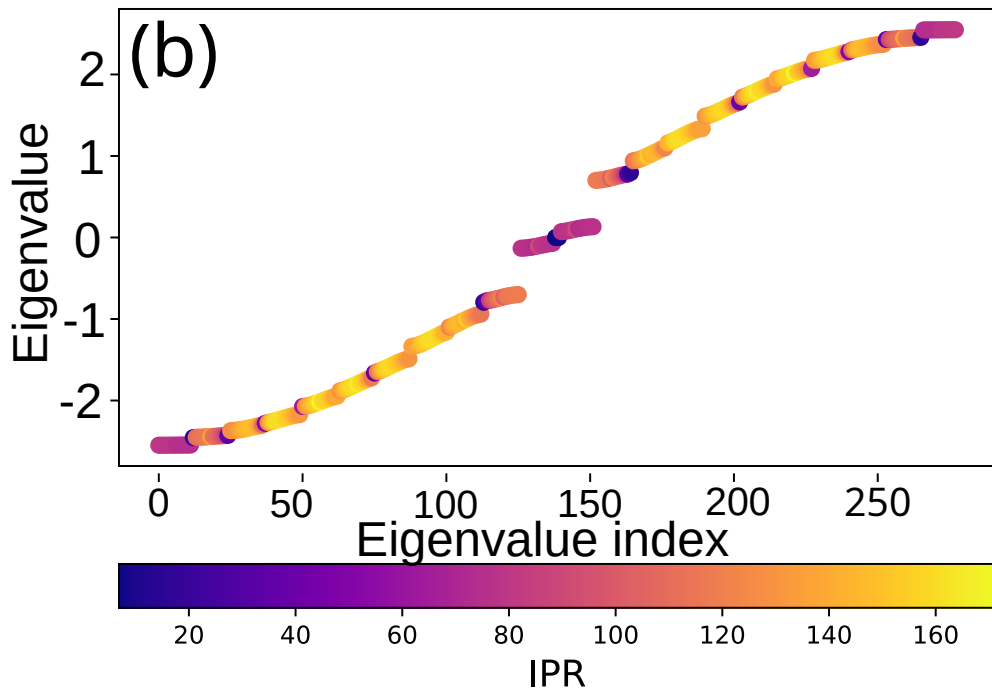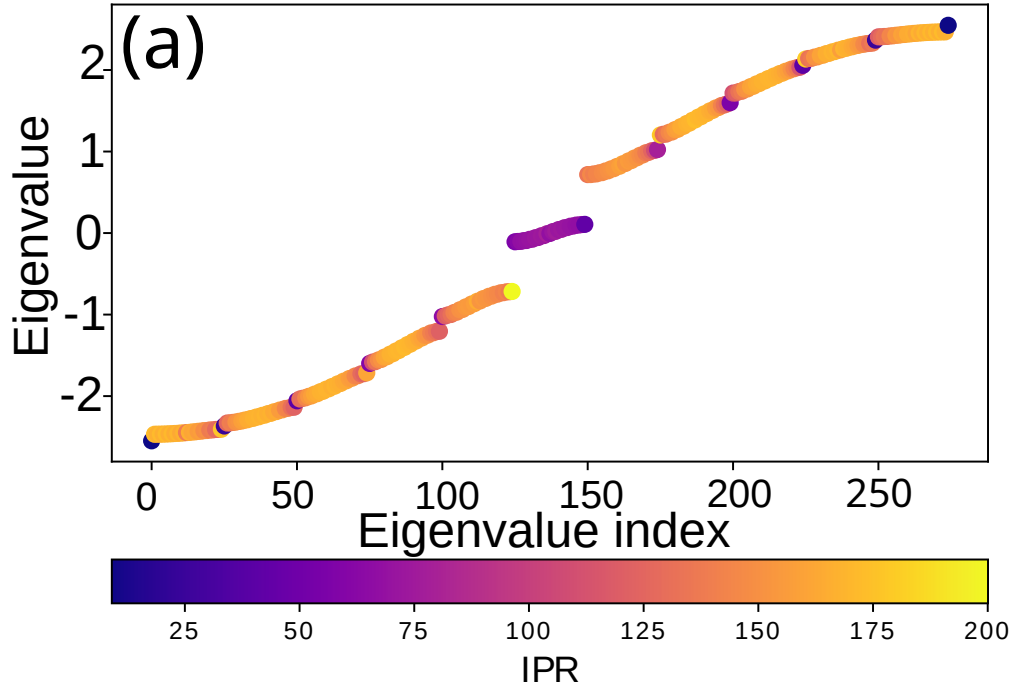
Figure 2.6: Eigenvalues of a finite superlattice (chain) of domain walls. In (a) all the sections of the superlattice have the same length, and the inner band resembles a simple metallic band. In (b) the superlattice has a bipartite geometry, with the inner band resembling the SSH model (in the topological phase).
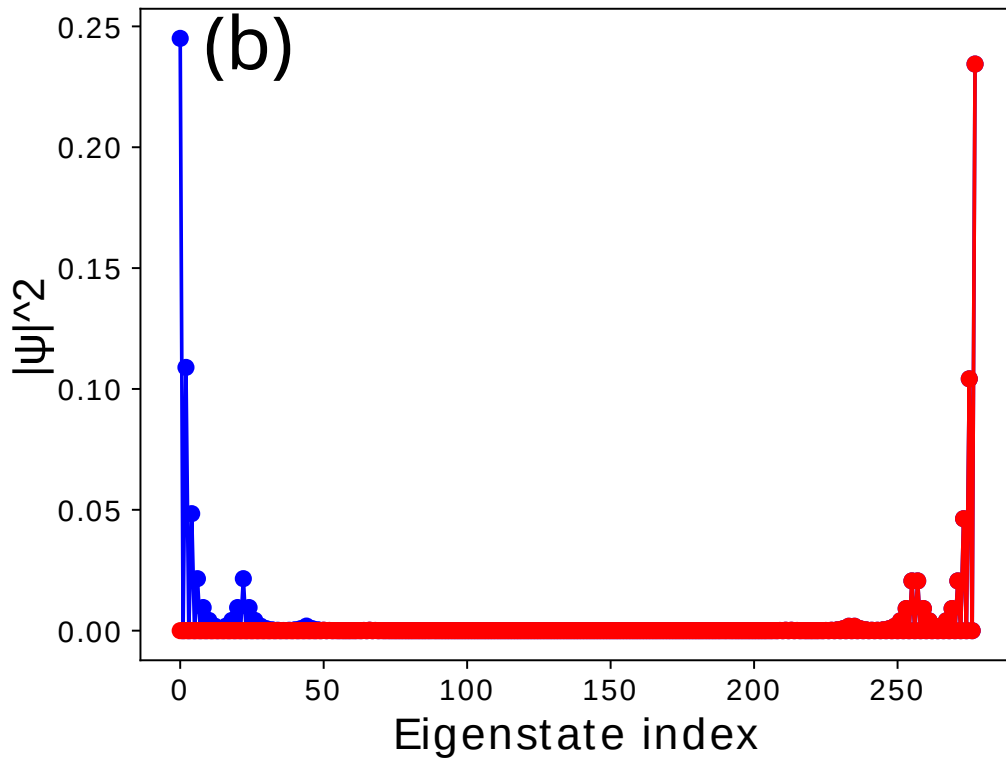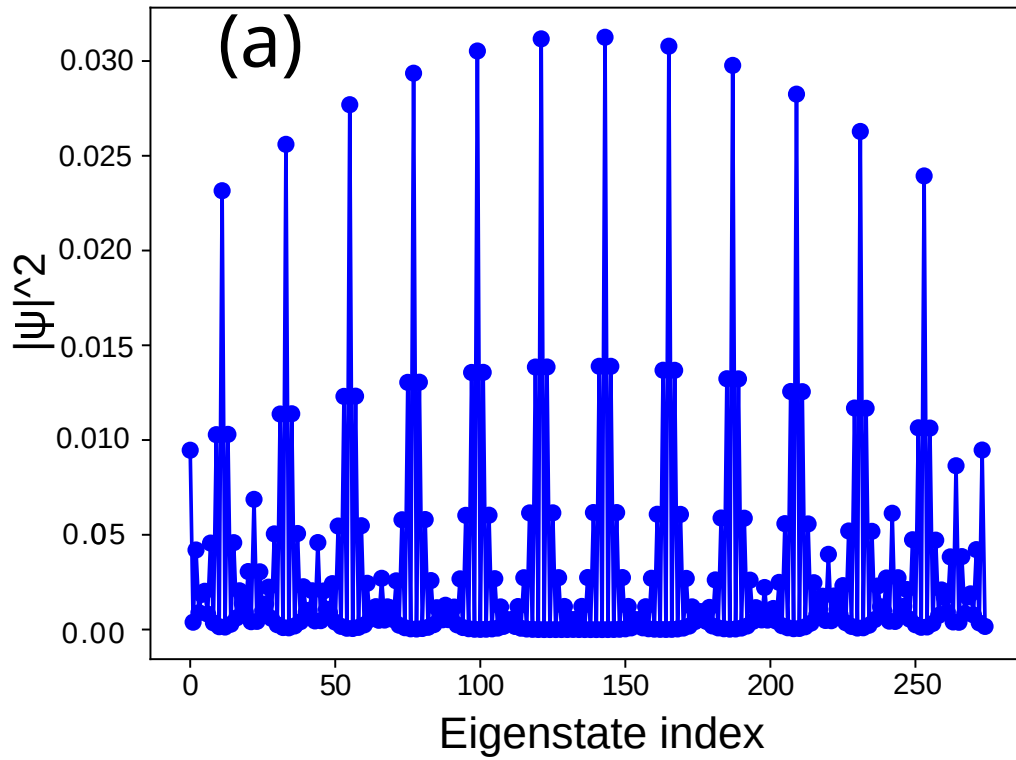
Figure 2.7: Eigenmodes of a finite superlattice (chain) of domain walls. In (a) all the sections of the superlattice have the same length, and the inner band resembles a simple metallic band. In (b) the superlattice has a bipartite geometry, with the inner band resembling the SSH model (in the topological phase). Only the modes at the Fermi energy were shown.

Chapter 3

Graphene

3.1 Crystalline structure of bulk graphene

If the position of an infinity set of discrete points are mathematically as:

$$R = n_1 \vec{a}_1 + n_2 \vec{a}_2,$$

we say that is a **Bravais lattice**, where n_1 are integers and a_i are vectors. But an hexagonal lattice is not *exactly* a Bravais lattice, because does not exist a linear combination that satisfies all positions. But if we include two atoms per lattice, we can construct the hexagonal array. This is called **lattice with a basis** and is a generalization of a Bravais lattice (similar to the bipartite lattice of the SSH model). In this description, all positions in the lattice are described by the relation:

$$\vec{R} = n_1 \vec{a}_1 + n_2 \vec{a}_2 + \vec{b}_i,$$

where b_i is a set of vectors $\vec{b} = \vec{b}_1, \vec{b}_2, ..., \vec{b}_n$. In this context, the *lattice vectors* for an hexagonal array, are:

$$\vec{a}_1 = \left(\frac{3a}{2}, \frac{a\sqrt{3}}{2} \right), \qquad \vec{a}_2 = \left(\frac{3a}{2}, -\frac{a\sqrt{3}}{2} \right),$$

with a the lattice constant, whose value depends on the distance of atoms. In the graphene context $a = \sqrt{(3)}a_{C-C}$, with $a_{C-C} = 1.4$ Å. And the basis $\vec{b}_1, \vec{b}_2$, are $(0,0)$ and $\left(\frac{a}{2}, \frac{a\sqrt{3}}{2} \right)$. So all orbitals in the plane can be plotted with this vectors. Finally, the Bravais lattice with a basis for an hexagonal geometry (honeycomb), in this context, for a graphene sheet, is:

$$\vec{R} = n_1 \left(\frac{3a}{2}, \frac{a\sqrt{3}}{2} \right) + n_2 \left(\frac{3a}{2}, -\frac{a\sqrt{3}}{2} \right) + \vec{b}_i, \tag{3.1}$$

with the set of two vectors:

$$\vec{b}_i = \left[(0,0), \left(\frac{a}{2}, \frac{a\sqrt{3}}{2} \right) \right] \tag{3.2}$$

To obtain the reciprocal vectors, we must remember that the non-coplanar vectors the reciprocal space are defined by:

$$a_j \cdot c_k = 2\pi\delta_{j,k}, \tag{3.3}$$

c_k the reciprocal lattice vector:

$$\vec{c_1} = \frac{2\pi}{3a}\left(1, \sqrt{3}\right), \qquad \vec{c_2} = \frac{2\pi}{3a}\left(1, -\sqrt{3}\right)$$

First, we remember that only the p_z orbital ($\pi - bands$) are being considered, because this approximation explains with sufficient accuracy the electronic properties of graphene at low energies. Besides, this atomic arrangement, with two atoms per site, have a translational symmetry, so the Bloch theorem is used in every atomic orbital ϕ_m to obtain the energy bands [51]:

$$\Phi_j(k, r) = \frac{1}{\sqrt{N}}\sum_{i=1}^{N}\exp\left(ik \cdot R_{i,j}\right)\phi_j(r - R_{i,j}),$$

with k the wavevector, $R_{i,j}$ the j orbital position of the $i - th$ unit cell.

Each wave-state Ψ is written as a superposition of each Bloch state (with M orbitals):

$$\Psi_m = \sum_{j=1}^{M}\psi_{j,m}(k)\Phi_j(k, r).$$

Solving the Schrödinger equation $H\Psi = ES\Psi$, with H the transfer integral matrix and S the overlap matrix. Now we consider S as the identity matrix, so the orbitals does not overlap with orbitals in other positions, only with themselves:

$$\begin{pmatrix} H_{AA} & H_{AB} \\ H_{BA} & H_{BB} \end{pmatrix}\begin{pmatrix} \psi_{j,A}(k) \\ \psi_{j,B}(k) \end{pmatrix} = E(k)\begin{pmatrix} \psi_{j,A}(k) \\ \psi_{j,B}(k) \end{pmatrix} \tag{3.4}$$

It is assumed that does not have directional interaction, so the energy interaction between the carbon A and the carbon B satisfies: $A \rightarrow B$ is equal to the energy $B \rightarrow A$, or put another way, the matrix is hermitian, so $H_{AB} = H_{BA}$ and the atoms in the unit cell are both equal $\implies H_{AA} = H_{BB}$. Assuming first neighbors interaction H_{AA} is the onsite energy:

$$H_{AA} = \frac{1}{N}\sum_{i}^{N}\langle\psi_A(r - R_{A,i})|H|\psi_A(r - R_{A,i})\rangle = \varepsilon_A$$

$$H_{AB} = \frac{1}{N}\sum_{i}^{N}\sum_{r=1}^{3}\exp\left(ik\delta_r\right)\langle\psi_A(r - R_{A,i})|H|\psi_A(r - R_{A,i} - \delta_r)\rangle = t$$

In the second equation the interior sum is over the three close neighbors of each atom.

The vectors δ_r connect each atom with the respective neighbors. Explicitly these vectors are:

$$\delta_1 = \frac{a}{2}(1, \sqrt{3}) \tag{3.5}$$

$$\delta_2 = \frac{a}{2}(1, -\sqrt{3}) \tag{3.6}$$

$$\delta_3 = -a(1, 0) \tag{3.7}$$

Without losing generality, the on-site energy can be set to zero because the two atoms are the same and we fixed the energy with respect this onsite potential. After applying the Bloch theorem, the reciprocal space Hamiltonian is

$$H = \begin{pmatrix} 0 & tf(k) \\ tf(k) & 0 \end{pmatrix}, \tag{3.8}$$

here $t = \langle \psi_A(r - R_{A,i})|H|\psi_A(r - R_{A,i} - \delta_r)\rangle$ and $f(k)$ are exponential that appear expanding the interaction between atoms in different unit cells:

$$f(k) = \exp(ik \cdot \delta_1) + \exp(ik \cdot \delta_2) + \exp(ik \cdot \delta_3)$$
$$= \exp(ik \cdot \delta_3)(1 + \exp(ik \cdot (\delta_1 - \delta_3)) + \exp(ik \cdot (\delta_1 - \delta_3))$$

Using this in $f(k)$:

$$\implies f(k) = \exp(-ik_x)\left(1 + 2\exp\left(ik_x a \frac{3}{2}\right)\cos\left(ik_y a \frac{\sqrt{3}}{2}\right)\right),$$

Finally, the energy is obtained:

$$E(k) = \pm t\sqrt{1 + 4\cos\left(ik_x a \frac{3}{2}\right)\cos\left(ik_y a \frac{\sqrt{3}}{2}\right) + 4\cos^2\left(ik_y a \frac{\sqrt{3}}{2}\right)} \tag{3.9}$$

Now we focus on the zone around the Dirac cones, where the conduction and valence bands intersect (the gap is closed). These points are called $K_\pm$:

$$K_\pm = \left(\frac{4\pi}{3}, 0\right),$$

expanding the $f(k)$ near this point and using $\vec{p} = \hbar k$:

$$f(k) = \exp(-ik_x)\left(1 + 2\exp\left(ik_x a \frac{3}{2}\right)\cos\left(ik_y a \frac{\sqrt{3}}{2}\right)\right)$$
$$\approx \left(1 + \frac{ip_y a}{\hbar\sqrt{3}}\right) + 2\left(1 + \frac{-ip_y a}{2\hbar\sqrt{3}}\right)\left(-\frac{1}{2} + -\frac{p_x a\sqrt{3}}{4\hbar}\right)$$
$$\approx \left(\frac{a\sqrt{3}}{2\hbar}\right)(px - ip_y).$$

18
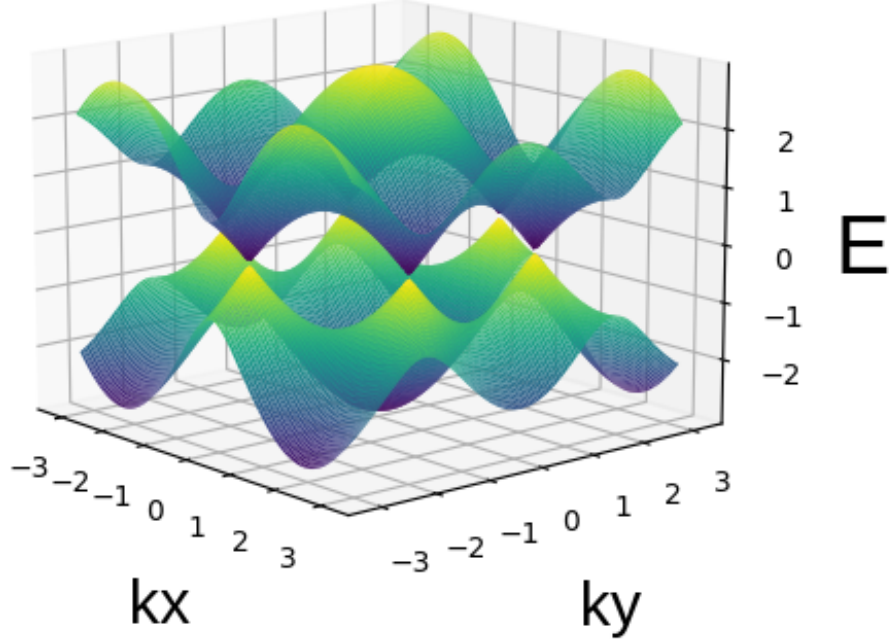
Figure 3.1: Bands for the graphene structure. Dirac cones can be seen where HOMO and LUMO intersect (valence and conduction bands intersect).

Replacing this algebraic expression in the Hamiltonian, we obtain:

$$H = \left(\frac{a\sqrt{3}}{2\hbar}\right) \begin{pmatrix} 0 & (p_x - ip_y) \\ (p_x - ip_y) & 0 \end{pmatrix} = v_F(p_x\sigma_x + p_y\sigma_y) = v_F\sigma \cdot p \qquad (3.10)$$

using the Fermi velocity $v_F = \left(\frac{a\sqrt{3}}{2\hbar}\right)$, we now obtain a Dirac like energy spectrum for a massless particle. Remember that the energy for a relativistic particle (modeled by Dirac equation), is:

$$E = \sqrt{(mc^2)^2 + (p_jc)^2}, \qquad (3.11)$$

if we set $m = 0$ and change the speed of light c for the Fermi speed, we obtain the same equation.

The previous item shows the relation of the energy in the low energy context. This provokes that the chiral symmetry or the helical operator appears. It is defined by:

$$h = \sigma \cdot \frac{p}{|p|}, \qquad (3.12)$$

19

This is an important consequence, because is useful to obtain some properties of relativistic particles without mass. One of them is the Klein tunneling. That is the absence of backscattering.

3.2 Graphene Nanoribbons and Nanotubes

In the previous section we study the case of thin layer of graphene. The honeycomb disposition was extended on the plane infinitely in two directions. We will now introduce the electronic properties of nanoribbons that will be useful for the next chapters.

Now, a direction of the graphene is truncated. So, the geometry is infinitely only in one direction, the other have a width with N atoms (N finite). Depending on the angle at which the tape is cut, different geometries will be generated. In the context of this research, only zig-zag and armchair-type borders will be used.
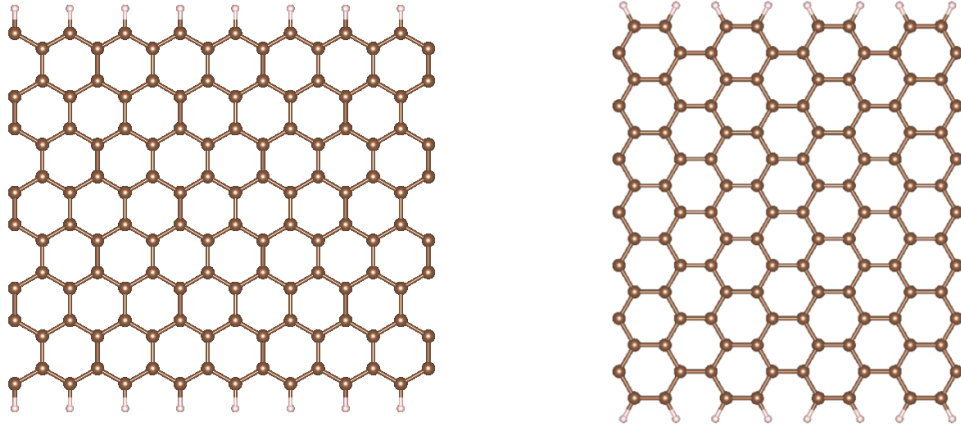
Figure 3.2: Graphene nanoribbons. The left panel shows a zig-zag termination, while on the right panel an armchair-type termination is whon (the edges are horizontal and saturated with H).

3.2.1 Zig-zag (ZGNR)

In this geometry, an interaction Hamiltonian can be written as:

$$H_{zig-zag} = \sum_{j=1}^{N-1} t a_{2j+1}^{\dagger} b_{2j} + t c(k_x) a_{2j-1}^{\dagger} b_{2j} + H.C, \qquad (3.13)$$

with $c(k_x) = 2\cos(k_x a/2)$. This Hamiltonian is diagonalized to obtain the bands of the system in reciprocal space. Regardless of the width of the ribbon, it is gapless.
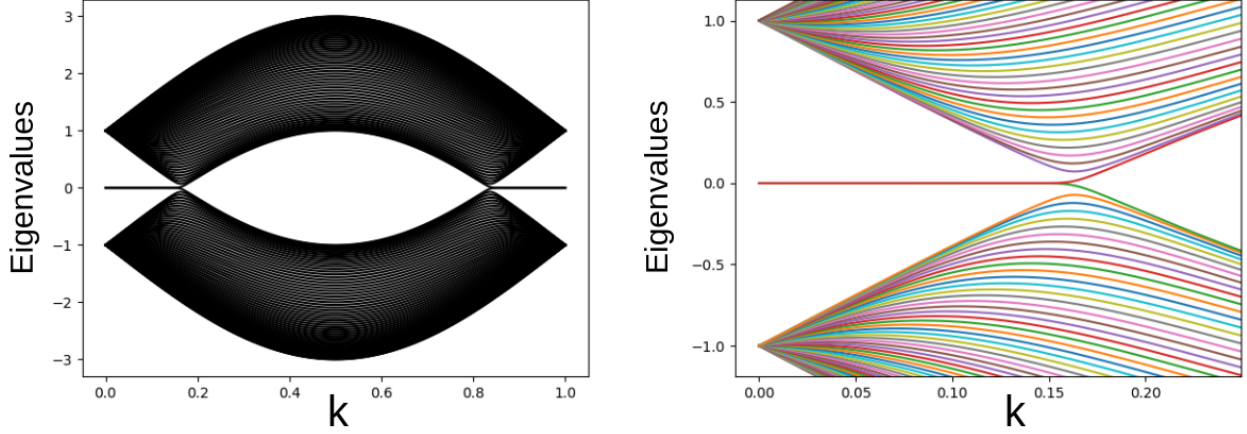
Figure 3.3: Typical bands of graphene nanoribbons with zig-zag termination.

3.2.2 Armchair (AGNR)

For different electronic applications [52], it is necessary to open a energy gap for graphene. It was specified that in the case of zig-zag termination, this condition cannot be fulfilled by changing its width. However, this situation changes in the termination of the armchair type. To understand this situation, the Hamiltonian of this geometry is:

$$H_{armchair} = \sum_{j=1}^{N/2} d(k_x)ta_{2j}^\dagger b_{2j} + ta_{2j+1}^\dagger b_{2j+1} + ta_j^\dagger b_{j+1} + H.C, \qquad (3.14)$$

Diagonalizing the system to obtain the bands, a gap opening can be seen depending on the width N of the tape. This electronic behavior can be classified as follows:

$$N = 3p \rightarrow Semiconductor(gapped).$$
$$N = 3p + 1 \rightarrow Semiconductor(gapped).$$
$$N = 3p + 2 \rightarrow Metallic(gapless).$$

basically, by boundary conditions, the one-dimensional reciprocal space of AGNRs with $N = 3p + 2$ touches the $K\pm$ points, resulting in a gapless system.

Furthermore, for each sub-classification, it can be seen that the energetic bandgap decreases with increasing width (see Figure 3.4).

Regarding the topological number associated with the armchair-type nanoribbon, it can be mentioned that this will depend on the termination of the unit cell. It will also depend on the width of the GNR, first identifying whether this quantity is odd or even. For more details on this topic, see the research by Ting Cao *et al.* [36]. The specific case of N-AGNRs will be covered in the next chapter.
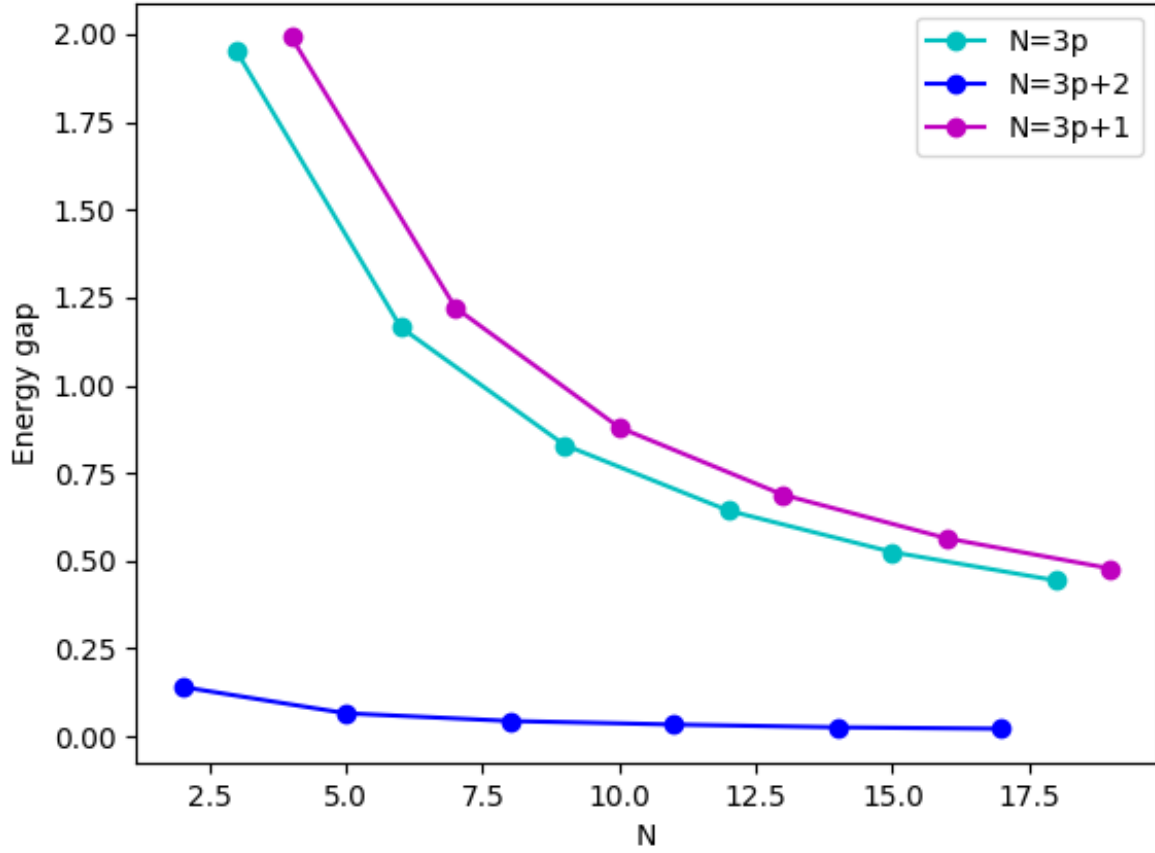
Figure 3.4: Variation of the energy bandgap as a function of the width of the armchair graphene nanoribbon.

3.3 Strain in AGNRs

As stated in the previous sections, to be useful in electronic devices, it is necessary to control the band gap of graphene band-gap. Different mechanisms have been proposed for this, such as the application of external electric fields, the generation of defects or the application of a strain.

Since this is one of the strongest materials, different experimental and theoretical studies have been carried out on the application of strain.[53] It has been verified that this mechanism generates a change in the energy band-gap. In this section we will elaborate into the theoretical foundations of strain in armchair and zig-zag geometries.

In general, the application of a strain changes the positions of each atom of the lattice. For a small strain, the new positions can be written in the new lattice vectors as [44, 54]:

$$a' = (I + a)\varepsilon, \tag{3.15}$$

With I the identity matrix, a the lattice vector without deformation and ε the deformation

tensor. This last term is written as a symmetric matrix:

$$\begin{pmatrix} \varepsilon_{xx} & \varepsilon_{xy} \\ \varepsilon_{xy} & \varepsilon_{yy}. \end{pmatrix} \qquad (3.16)$$

Positive values imply an elongation of the system, while negative values imply compression of the lattice. There is also the possibility of using a shear strain. On the other hand, some authors write this matrix diagonalized in a base such that the terms that make it up imply strain in the armchair and zig-zag directions ([44], while other research has generalized this tensor using a deformation at different angles ([55]).

This change of the lattice generates a displacement of the points K, where the Dirac cones intersect, to a new position K'. In this way, differences in the energy band gaps of each graphene nanoribbon arise because the GNRs can become closer or farther from the K points. These changes are related to the topological phase of the AGNR: one phase experiences a increase of the band gap with strain, but the other experiences a decrease of its band gap. Figure 3.5 shows this for a couple of N-AGNRs.
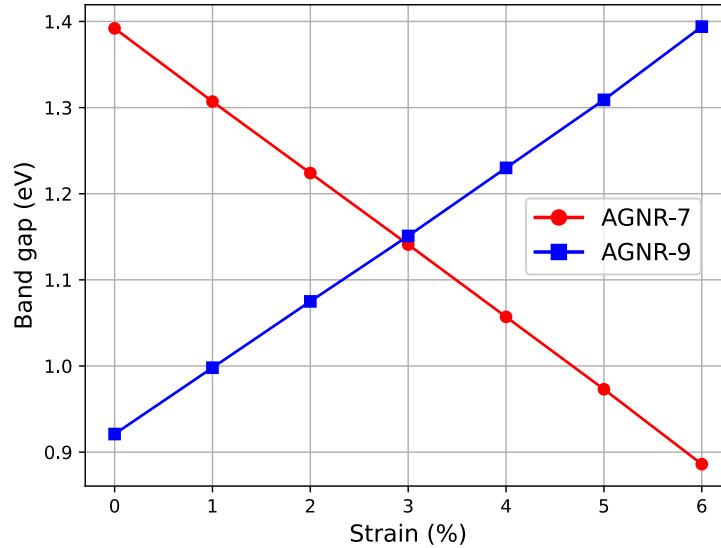
Figure 3.5: Evolution of the band gap as a function of strain. The AGNRs are fully relaxed (the only constraint is the strain). The $7 - AGNR$ and $9 - AGNR$ belong to different topological phases, hence their band gaps have the opposite behavior with strain.

Is important to clarify that in a experimental setup there would be a three dimensional strain and not two dimensional, as stated in equation (3.16).

Chapter 4

Interface States in Modulated AGNRs

Advances in techniques for obtaining GNRs in their different geometries, mainly through bottom-up synthesis, have made it possible to advance in different applications of this material. This technique has allowed to have control in the terminations and width [36]. In this context, in 2017, Ting Cao *et al.* established a method to determine the topological invariant in armchair graphene nanoribbons with different types of terminations, either zig-zag or bearded. Subsequently, Rizzo and collaborators[34] synthesized a superlattice of graphene ribbons and in parallel, an investigation by Gröning *et al.*[2] obtained superlattices of this material, being able to measure topologically nontrivial edge estates by varying parameters in the terminations of the superlattices.

In this chapter, the basic physics of a AGNR superlattice will be established and the theory related to experimental findings of Rizzo [34] and Gröning [2] will be developed.

4.1   Junction states

The implications of joining two AGNRs of different size were developed by Ting-Cao *et al.* [36] Depending on the atomic details of each junction, a localized interface state may appears. As an example, consider an AGNR of width $N = 7$ ($N = 3p+1$) and another of width $N = 9$ ($N = 3p$), both are semiconductors. There are more than one way to make an interface among both AGNRs, it can be symmetric with respect to the center of the width of the ribbon, or not. Depending on this specific arrangement, substantial differences arise at the interface. In the symmetric case there is a localized state of energy close to zero (*i.e.* the Fermi energy), while in the other case there is no such state. This is because there a different termination at the junction of the ribbons defines a have different topological number within each AGNR segment.

Gröning *et al.* [2], developed a strategy to recreate a SSH-like chain using junction states made with AGNRs. They restrict the possible junctions to only two types -*staggered* and *inline*- which can be synthesized, see Figure 4.1. In this way, the emergence of a localized state can be deduced just from the width of each section: it should appear if the width of
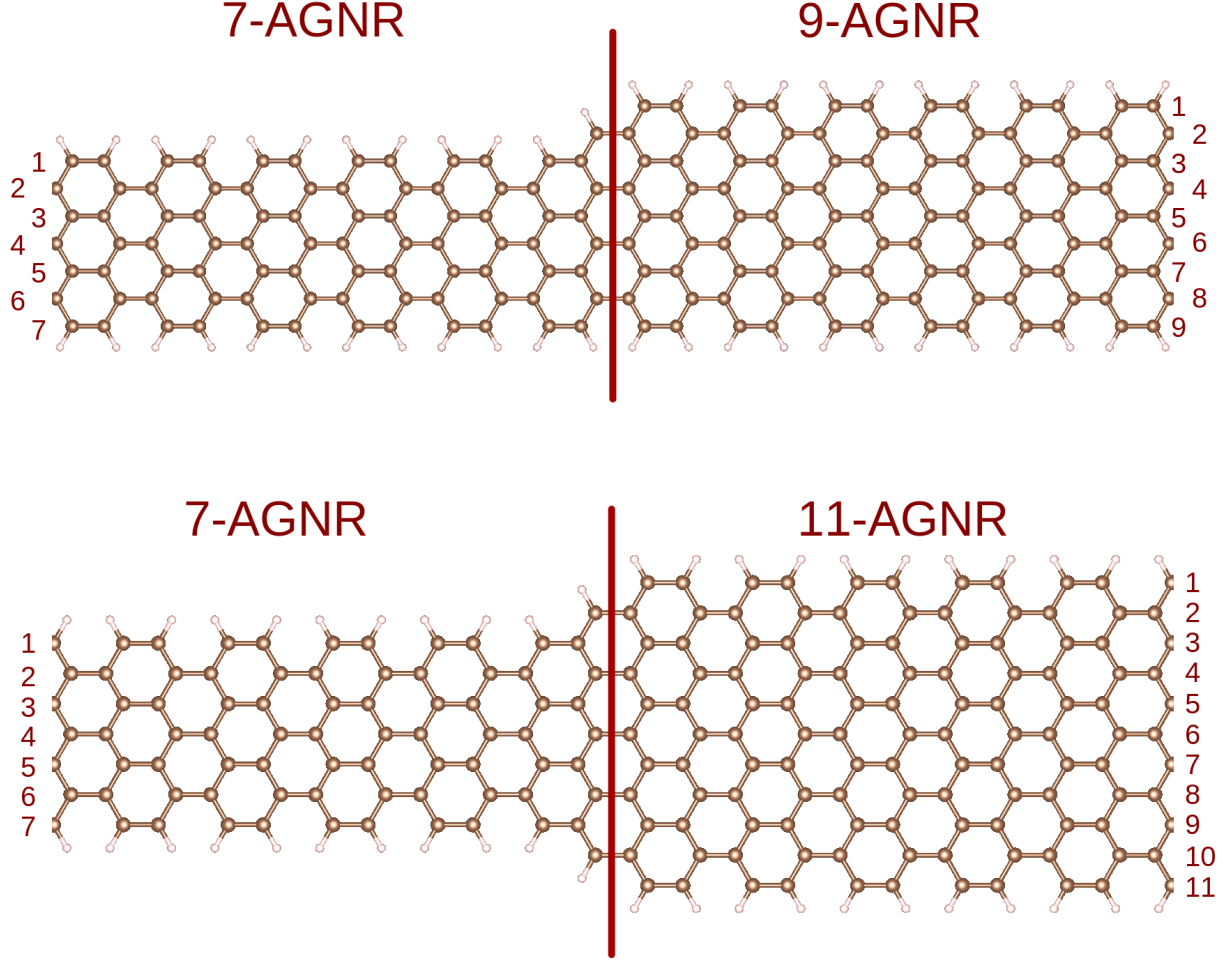
Figure 4.1: Upper (lower) panel, shows the *staggered* (*inline*) type interface. In the *staggered* (*inline*) intheface, the wider region is 2 (4) atoms wider than the thinner part.

each segment belongs to different insulating classes. These different classes are defined by the width N of the AGNR:

$$N = 3p \qquad (semiconductor\ type\ 1) \tag{4.1}$$

$$N = 3p + 1 \qquad (semiconductor\ type\ 2) \tag{4.2}$$

$$N = 3p + 2 \qquad (metallic), \tag{4.3}$$

with p an integer.

Using the DFTB+ package,[56] the bands and wave functions are obtained. The states close to zero energy are identified. In the case of *staggered* type junctions, localized states are obtained at the junction of $7 - AGNR$ and $9 - AGNR$, since both insulators belong to the families $N = 3p + 1$ and $N = 3p$, respectively, see Figure 4.2. In the other cases shown, one of the AGNRs is metallic ($N = 3p + 2$) and extended states are found.
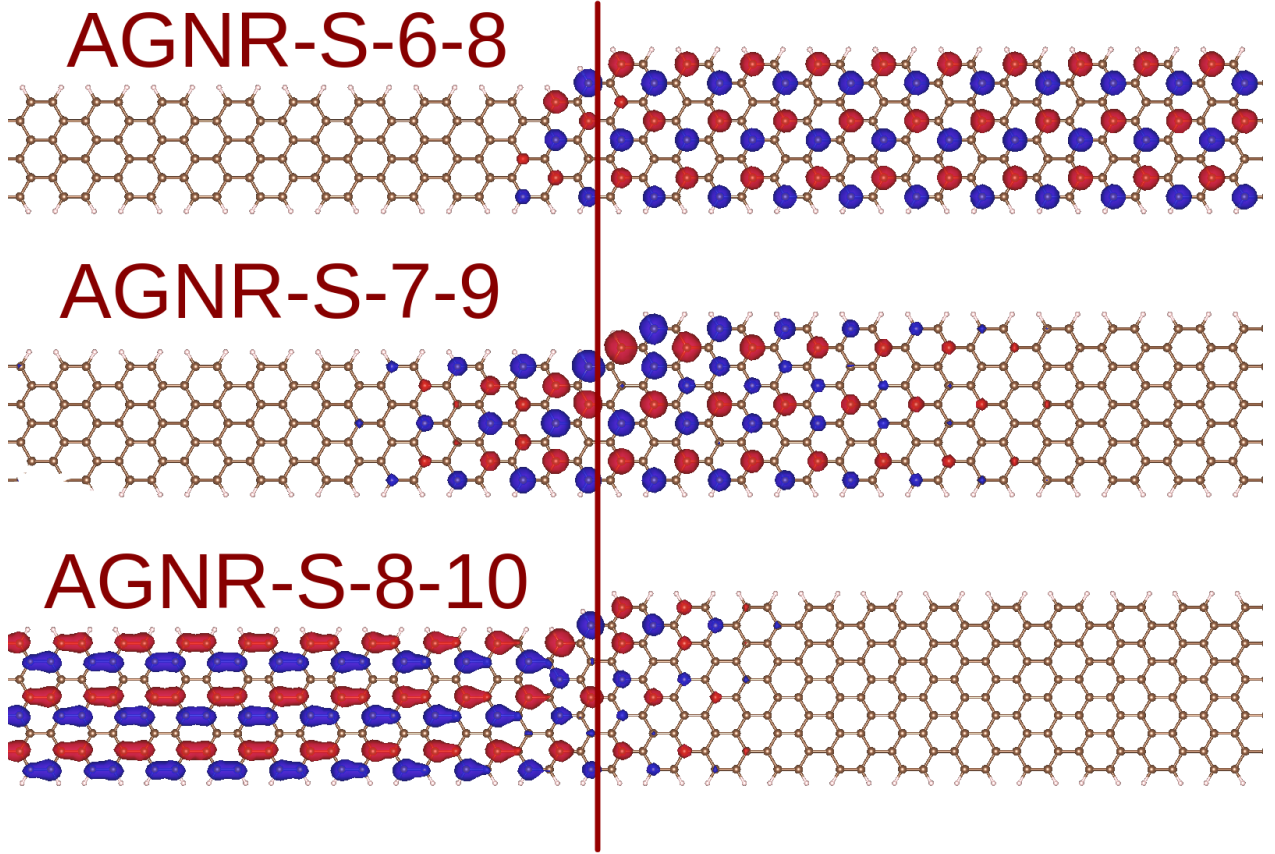
Figure 4.2: Near-zero energy states of several possible junctions in the staggered family. A localized state can be seen at the interface between 7-AGNR and 9-AGNR, both insulators, but with different topological number. When one of the AGNRs is metallic, $N = 3p + 2$, the low energy states are extended along the metallic region.

In their publication,[2] Gröning *et al.* propose an analogy with the SSH model. To understand it, in figure 4.4 there are two interface states separated by a finite distance. These states, $\langle R|$ and $\langle L|$ overlaps. And a small interaction develops.
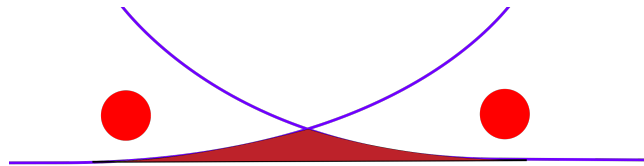
Figure 4.3: Scheme of the overlap of two localized states. They interact with a finite energy that will depend on the distance between them.

The interaction energy is given by $t_n = \langle L|H|R \rangle$, in complete analogy with the domain wall defects in the SSH superlattice exposed in the previous chapter, where a superlattice is derived from these interactions.
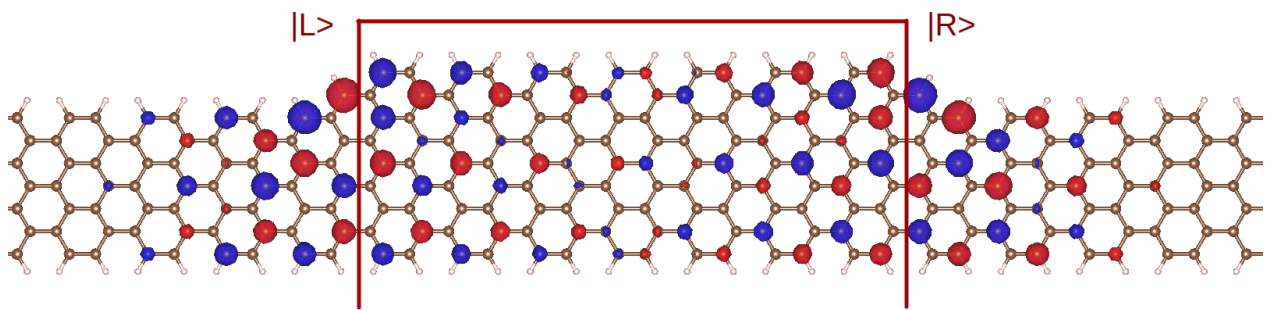
Figure 4.4: Interaction between junction states. The localized states do hybridize originating a pair oof bonding and antibonding states. In the figure the antibonding state (odd parity) state is shown.

Chapter 5

AGNR superlattices

As stated in the previous sections, an AGNRs can be classified in one of three different families, according to the their width N, $N = \{3p, 3p + 1, 3p + 2\}$ (where p is a positive integer)[20]. According to their Zak phase, the families $N = 3p$ and $N = 3p + 1$ belong to a different topological class[36], while the $N = 3p + 2$ is predicted to be metallic (excluding a small gap opening due to finite-width effect). Indeed, the one-dimensional k-points of a $N = 3p + 2$ AGNR passes over the K and K' points of graphene (graphene's Dirac cones location), explaining its lack of a band-gap.[57] In the other families of AGNRs the band-gap decreases with N.

At the interface between $N = 3p$, $N' = 3p + 1$ AGNRs, due to their different topological invariant,[36] a localized state within the band-gap must appear (usually called a 'topological' state). For instance, Rizzo *et al.* found these states in the interface between 7-AGNR and 9-AGNR.[34] The penetration of these states into the AGNR bulk is inversely proportional to the system band-gap, *e.g.* the topological state penetrates deeper into a 9-AGNR region than into the 7-AGNR. In the case of a superlattice of AGNRs of different widths, these localized states hybridize with each other, forming extended states that conserve some of the properties of their constituent localized states. Generally, the localized states penetrate deeper into one region than into the other, allowing the formation of a bipartite lattice in the low-energy description (*i.e.* analogous to a diatomic chain), even if each AGNR segment has the same length. The physics of such a low-energy description is captured by the SSH model, which has two gapped phases, trivial and topological. Notably, one of them predicts the existence of topologically protected edge states. Therefore, in the superlattice of different AGNRs, the edge states are made from SSH-like topologically derived interface states or superlattice states[42]. In this work we extend the work by Gröning *et al.* including strain, which can modify topological states.

In the following, we will use Gröning *et al.* notation.[2] The modulated AGNRs are labeled as N-AGNR-$S(n, m)$, or N-AGNR-$I(n, m)$ where N stands for the backbone width, n is the length of the wider region, m is the distance between the wider regions, and S or I defines the ribbon as 'staggered' or 'inline'. The wider regions has width $N' = N + 2$ and $N' = N + 4$ for the S and I cases, respectively. See Fig 5.1.

In the remainder of this chapter, we will restrict to just two different AGNR superlattices,
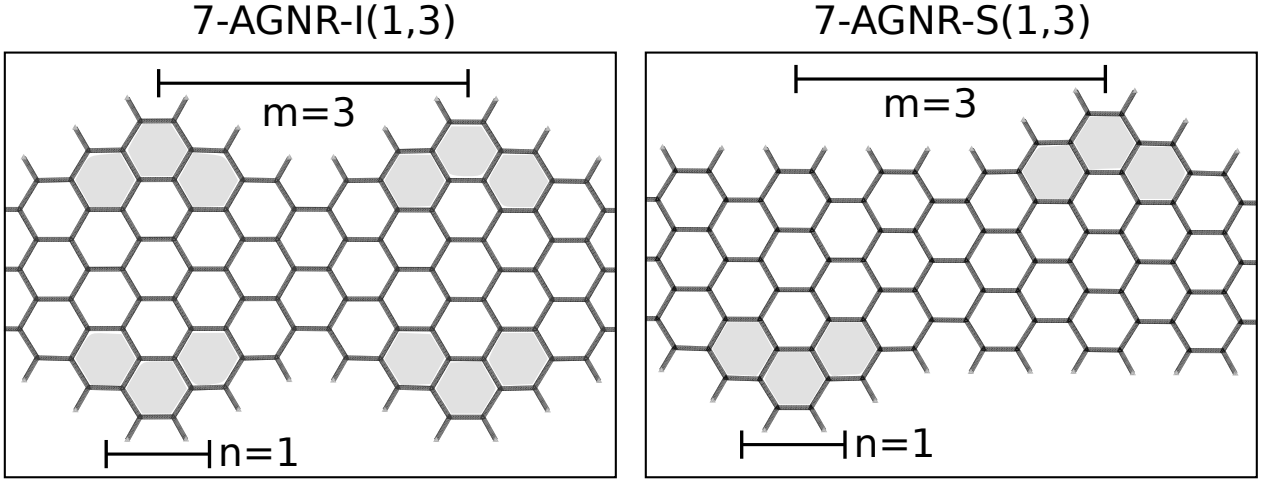
Figure 5.1: Schematic of the N-AGNR-I(n,m) and N-AGNR-S(n,m) superlattices. N is the width in C atoms of the *backbone*, *i.e.* removing the shaded regions. The shaded regions have a width $N' = N + 4$ for the I (inline), and $N' = N + 2$ for the S (staggered) conformations. The indexes n, m are the length of the wider region and the distance (in unit cells of the backbone AGNR) between adjacent wider regions, respectively. The panel of the $I(S)$ system shows two (one) unit cells.

7-AGRN-I(1,3) and 7-AGNR-S(1,3). Recently, both systems were experimentally studied by Gröning *et al.*[2] where the low-energy states were described by a superlattice realization of the SSH model. While 7-AGNR-S(1,3) is in the trivial phase of the SSH model, 7-AGNR-I(1,3) has a non-trivial phase resulting in localized states at its edges. These edge states are protected by the chiral symmetry of the Hamiltonian (*i.e.* they should be degenerated as long as the on-site energy of each interface of the superlattice is the same), and they are sublattice polarized (see Fig. 5.2).

In addition to the possible presence of the SSH-like topological states (derived from the superlattice geometry), the AGNRs have other topological states: they come from the sublattice split zig-zag borders, and they are not related to the superlattice geometry. To distinguish between both types of topological states, we follow the approach of Gröning *et al.* using an extended backbone, without the modulation. Fig. 5.2 shows this type of edge, while in both cases, the zig-zag border has topological states, only in 7-AGNR-I(1,3) there are topological states at the end of the superlattice. At the Fermi energy of this system, four states exist with almost the same energy. Two are at the (left and right) superlattice boundary, and another two at the backbone's zig-zag edge. These states have a residual interaction, and they hybridize due to finite-size effects.

Meanwhile, we have restricted the discussion to the Zak phase arising from the effective SSH model, the "full" topological invariant $\mathbb{Z}_2$ should be calculated from the entire occupied manifold:

$$(-1)^{\mathbb{Z}_2} = e^i \sum_n \gamma_n \tag{5.1}$$

where γ_n is the integral of the Berry connection over the Brillouin zone, and n runs over

7-AGNR (backbone) | 7-AGNR-I(1,3) superlattice, left edge

7-AGNR (backbone) | 7-AGNR-S(1,3) superlattice, left edge
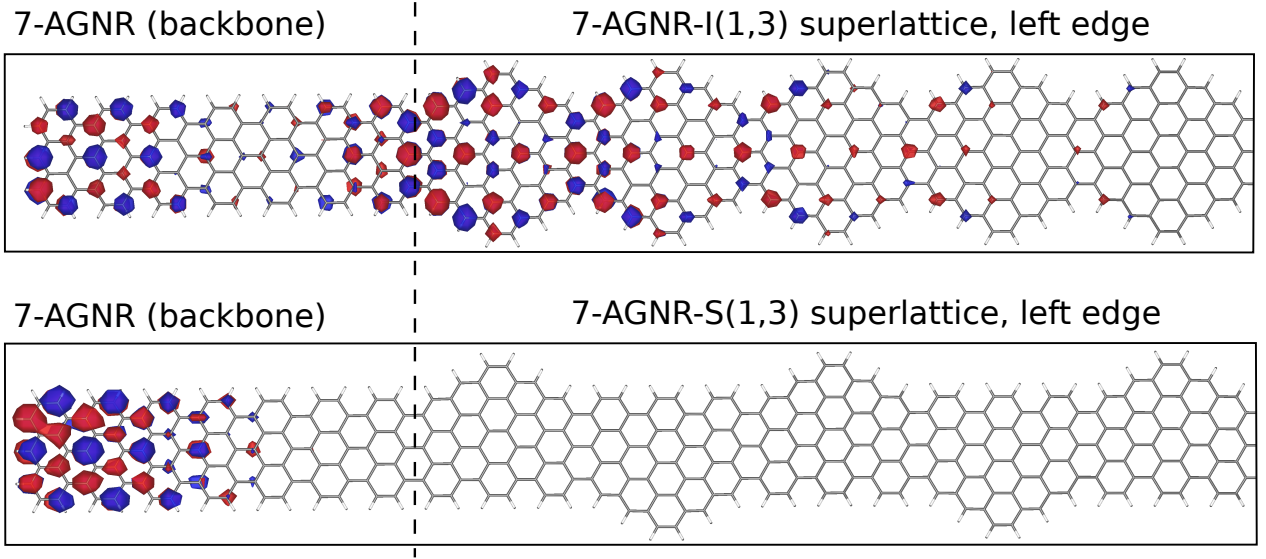
Figure 5.2: Model of the left edge of finite superlattices 7-AGNR-I(1,3) and 7-AGNR-I(1,3). The dashed line marks the border of the superlattices, connected to finite 7-AGNR regions. The whole system is much larger, and only the left edge is shown. The wave-functions of the topological states are shown. The 7-AGNR-I(1,3) and 7-AGNR-S(1,3) have a topological and a trivial phase, respectively, reflected in the existence or lack of localized states at the superlattice edge (dashed line). At the edge of the 7-AGNR there is another topological state, not related to the superlattice. In 7-AGNR-I(1,3), both states form a linear combination, and only one of them is shown.

the occupied bands. The invariants obtained this way are $\mathbb{Z}_2 = 1$ for 7-AGNR-S(1,3), and $\mathbb{Z}_2 = 0$ for 7-AGNR-I(1,3), converse to the invariants obtained from just the SSH bands. The topological invariant of the backbone, 7-AGNR, is non-trivial $\mathbb{Z} = 1$, explaining its edge states at the very end of the samples, and why the full superlattice follows the SSH scheme (presence/absence of edge states at the superlattice's edges). In the remainder we will stick to the simpler picture obtained just from the SSH bands. The interested reader can find more detail in the supporting information of Gröning *et.al.* [2].

5.1 Mechanical Properties of a Modulated Superlattice

Mechanical properties of any material become relevant every time a technological application is intended, since mechanical deformation can lead to changes in electronic properties, and plastic deformation and fracture can limit the range of applicability of the material[58]. In this section we analyze the mechanical response of 7-AGNR-S(1,3) and 7-AGNR-I(1,3) structures to a longitudinal uniaxial tension, and compare the results with the same test on 7-AGNR and 11-AGNR samples, which represent the narrowest and the widest versions of uniform width AGNR. We use classical molecular dynamics (MD), and details are given in section Methods.

Figure 5.3 displays the Stress-Strain curves for all four cases. The unmodulated AGNR show the typical behavior seen for GNR [53]: an initial linear elastic region, followed by a
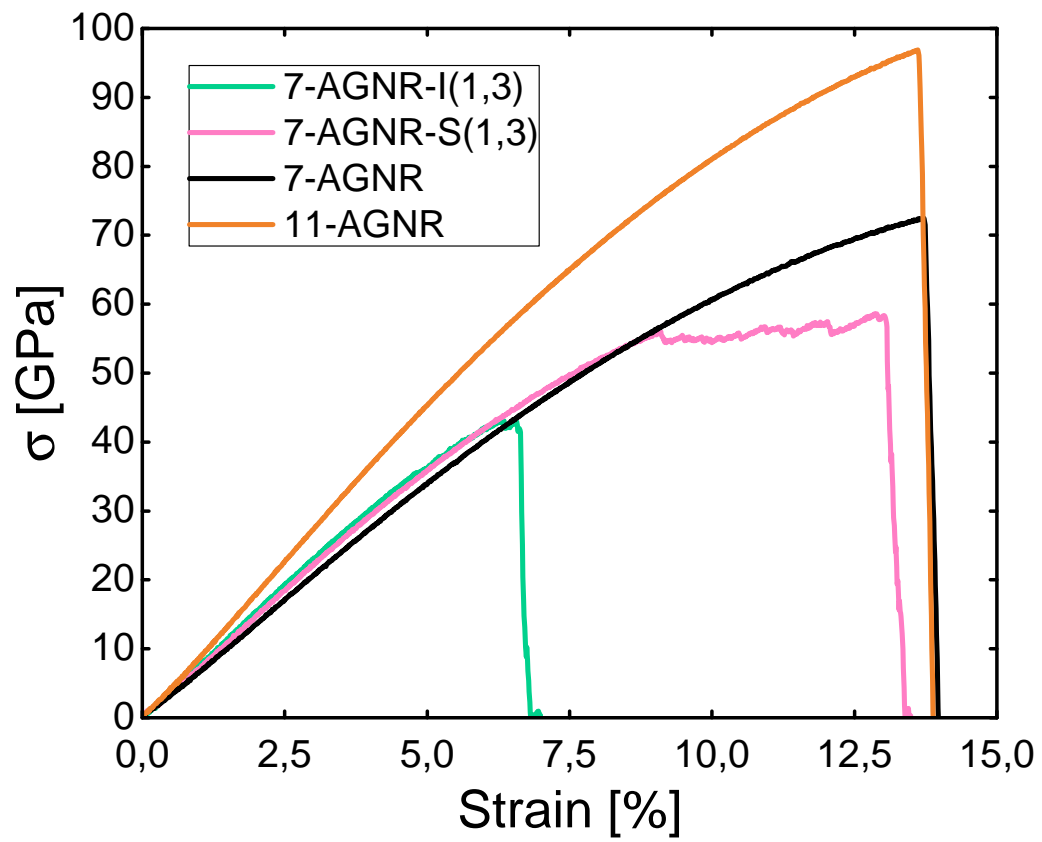
Figure 5.3: Stress-Strain curves for uniaxial deformation of the 7-AGNR-S(1,3) and 7-AGNR-I(1,3) superlattices. Results for the 7-AGNR and 11-AGNR are also shown.
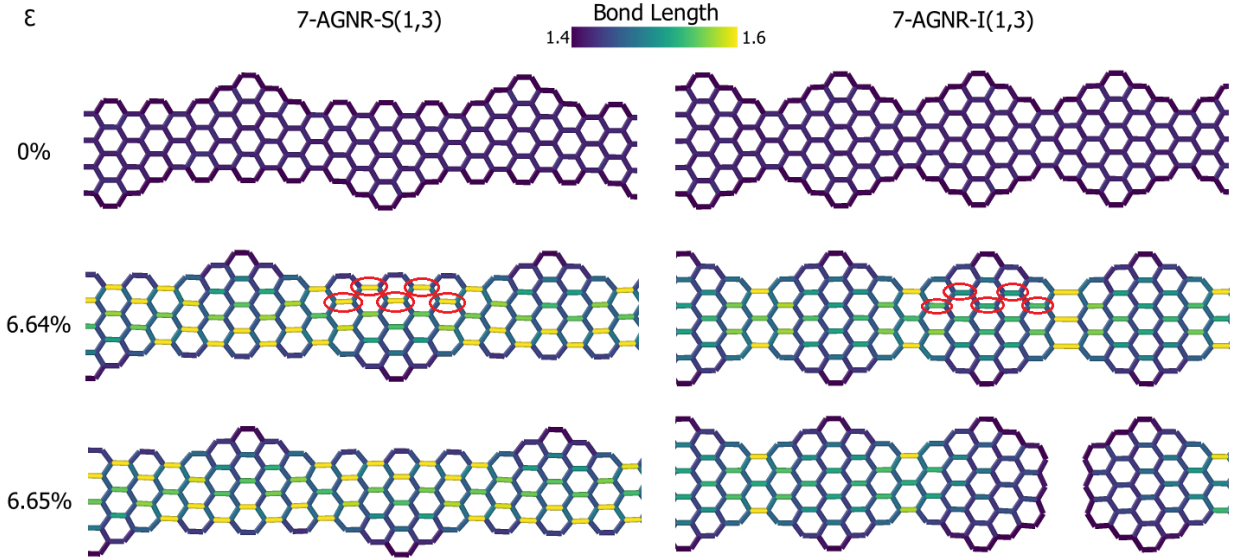
Figure 5.4: Snapshots showing deformation stages around the fracture strain for the 7-AGNR-I(1,3) superlattice, compared to the same strains for the 7-AGNR-S(1,3) superlattice. Some relevant spatially equivalent bonds are enclosed in red.

non-linear elastic region, ending in brittle fracture. The elastic module depends on ribbon width [53], but they both fracture near 13.8% strain. The elastic modulus of both modulated 7-AGNR is similar to the one for the 7-AGNR unmodulated ribbon. The 7-AGNR-I(1,3) case is similar overall to a typical AGNR, but modulation leads to a much lower fracture strain, at 6.7%. The 7-AGNR-S(1,3) displays an extended plastic region. This is because bonds between nanoribbon sections that give modulation are not broken, but extremely weak because they are stretched beyond 0.2 nm, which is the usual bond-breaking length for C nanostructures [59]. This allows the fracture strain to reach a value of 13.1%, close to the one for the unmodulated ribbons.

The fracture mechanism always takes place in the thinner regions (*i.e.* with the same width as the backbone) of the superlattice. In the Supplementary Material, the fracture mechanisms are displayed in detail for both modulated width AGNRs in Figures C.1 and C.2. Thinner regions allow stress concentration leading to bond fracture, while wider regions can distribute strain energy amongst more bonds. Figure 5.4 allows us to visualize why the 7-AGNR-I(1,3) superlattice presents a fracture strain much lower than the 7-AGNR-S(1,3) case: the region between different segments generating modulation in the "inline" case allows for larger bond elongation leading to fracture. The "staggered case" allows for a different bond-strain distribution which defuses fracture, as shown by the bonds circled in red. These simulation results indicate that modulated AGNR can withstand strains larger than those required in most technological applications, which are typically only a few percent [60, 61].

5.2 Strain and Electronic Structure of Superlattices.

Before discussing the results of the superlattice under axial strain, let us summarize what is expected in N-AGNRs (*i.e.* without the superlattice geometry). In AGNRs, the reciprocal space is just a one-dimensional projection that may or may not be commensurate with the position of the Dirac cone, dividing the N-AGNRs into three groups: one metallic ($N = 3p + 2$), and two families of insulators ($N = 3p, 3p + 1$). Under axial strain, the Dirac cone of graphene moves apart from the $K(K')$ points, hence the distance of the different k-lines (of different N-AGNR families) to the Dirac cones is shifted too. Regarding the band gap under uniaxial strain, it increases for $N = 3p + 2$ and $N = 3p$ AGNRs, while it decreases for $N = 3p + 1$ AGNR[44, 62]. For instance, without any strain the band gaps of 7- and 9-AGNR are $\Delta E_7 \approx 1.38$ eV and $\Delta E_9 \approx 0.92$ eV, respectively. As the 7- and 9-AGNR belong to different families ($3p + 1$ and $3p$), it is expected that an axial strain will decrease ΔE_7 but increase ΔE_9. We calculated that under a strain of $\sim 3\%$ both band gaps are the same $\Delta E_7 = \Delta E_9 = 1.15$ eV. For a larger strain the larger band gap correspond to 9-AGNR ($\Delta E_9 > \Delta_7$). This critical strain is much lower than the fracture strains found in 5.1. In the following, we will discuss the case of the interface between two N-AGNR under strain, and then the case of a superlattice.

To understand what to expect in a more complex AGNR, we will make a couple of assumptions: *(i)* the strain is uniform, and *(ii)* the regions of the AGNR sections are long enough to have well-defined *local* properties (*e.g.* a local band gap). Let us start by considering the 7/9-AGNR interface, where a localized state appears. The edge state's penetration length (ε) through the 7- and 9-AGNR regions (ε_7 and ε_9, respectively) depends directly on the *local* band gap of each region ($\Delta E_{7/9}$) as $(\varepsilon_{7/9})^{-1} \propto \Delta_{7/9}$. The interface of both AGNR systems has a critical point at a strain of $\sim 3\%$, where the band gap in both systems is the same and, consequently, the penetration lengths are also equal ($\varepsilon_7 = \varepsilon_9$). Below this critical strain, the penetration length meets $\varepsilon_7 < \varepsilon_9$, changing to a $\varepsilon_7 > \varepsilon_9$ for values greater than 3%.

For a superlattice geometry, for example if we consider evenly spaced 7- and 9-AGNR regions, every interface state hybridizes with its corresponding adjacent interface state. In a low energy description, this hybridization can be considered a hopping between two interface states proportional to their penetration length, $t_N \propto e^{-L/\varepsilon_N}$, where $N = \{7, 9\}$ and L is the length of each region. The hopping between edge states is the foundation of the model at low energies, and an SSH-like effective Hamiltonian can be constructed with its different topological phases.[42] In the pristine case, for uniform strain up to 3%, the band gap of the 9-AGRN is smaller, which means $t_7 > t_9$ in the low energy model. For the critical strain, $\sim 3\%$, both hopping strengths should be the same. Furthermore, for the last case, when the uniform strain exceeds 3%, the situation is reversed, obtaining $t_7 < t_9$. Interpreting this on the light of the SSH model, the transition in the hopping strength due to uniform strain implies a topological transition, resulting in new topological edge states corresponding to the superlattice geometry. It is worth remarking that we used some strong assumptions in this discussion, and the critical strain for the topological transition could be different. For instance, Fig. 5.4 shows non-uniform strain near fracture. However, the mechanism explaining the emergence of a topological transition should remain valid.
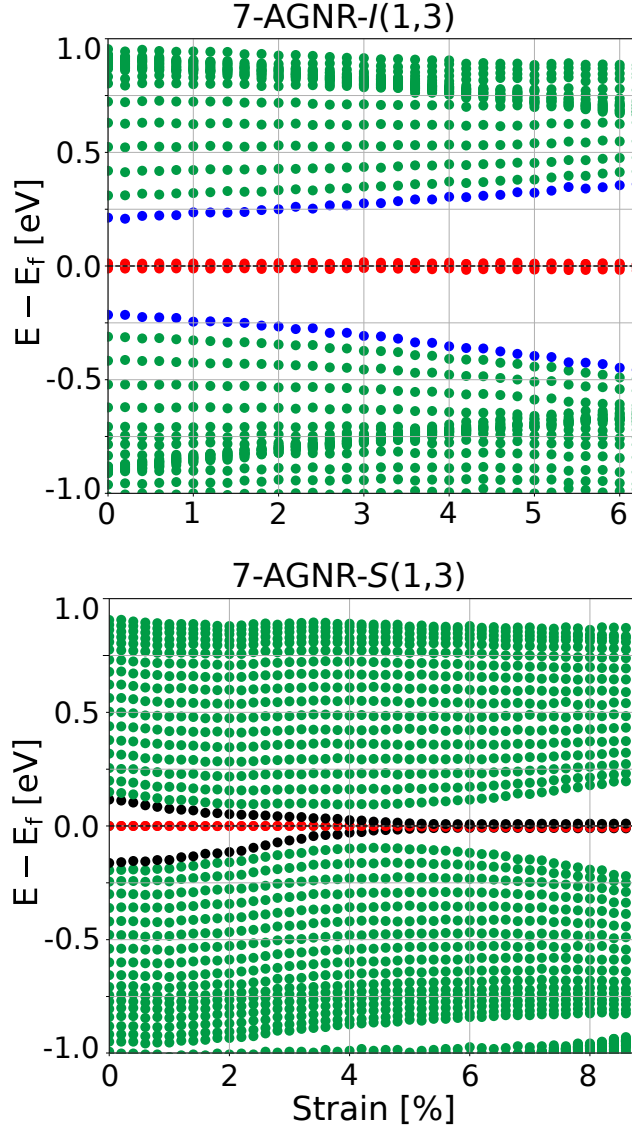
Figure 5.5: Evolution of the energy levels as a function of strain. The topological edge states are very close to $E = E_F$. In the 7-AGNR-I(1,3) there are four states colored red (two of them come from the zigzag borders). The 7-AGNR-S(1,3) superlattice has two topological states (colored red) from the zig-zag edges; meanwhile two bulk energy levels become topological at a strain close to 5% (colored black). Two bands are colored blue only to make Fig. 5.7 clearer.

For the electronic properties of the superlattice, we are interested in the region that precedes the fracture process. The evolution of the energy levels with the applied strain is shown in Fig. 5.5. All the levels shown are derived from the superlattice SSH-like states (the graphene bulk-bands are beyond this range). The first case under study is the 7-AGNR-I(1,3) superlattice. The system can be described as an SSH model in the topological phase for low energies, expecting two states in the Fermi energy. Further, two more edge states are contributed by the zig-zag termination in the edge [63]. The red dots in the upper panel of Fig. 5.5 are the practically fourfold-degenerate edge states at the Fermi energy, and there is a small hybridization between zig-zag and topological edge states. As a non-zero uniform strain is applied in the edge states, the SSH bulk-like bands move away from the Fermi energy. This behavior in 7-AGNR-I(1,3) is expected due to lack of changes in the topological phase in the low energies SSH-like model, and it does not break any symmetry required for the appearance of these states, including the zig-zag edge states (at the end of the extra backbone).

The counterpart system, on the trivial phase without strain, is the 7-AGNR-S(1,3). The first substantial difference is the absence of two edge states in the Fermi energy due to this trivial phase. Without strain, the bottom panel in Fig.5.5 shows the two-fold degenerated edge states coming from the zig-zag edge termination in the Fermi energy. Additionally, the green dots show trivial bands coming from SSH bulk-like states, and they approach or move away from the Fermi energy depending on whether the strain is less than or greater than $\sim 4.5\%$. As with the previous case, the zig-zag edge states do not show significant changes when the strain increases. However, at a certain critical point (between 4% and 5%), two additional states begin to coexist at the Fermi level (black dots in the figure), and there is also an edge localization. The origin of these states can be explained as a change in the phase of the effective SSH model and originates due to the changes from one region to another (7- or 9-AGNR) of the hopping strength magnitude between adjacent boundary states. This change from a trivial to the topological phase implies the emergence of topological states at the superlattice edge and remains very stable against the increase of strain. Fig. 5.6 shows the wavefunction of one of the levels involved in this transition, the sublattice polarization increases with strain. At a strain 5.0% (panel c), even in the region without sublattice polarization it is small. The transition is not obvious from this figure, therefore in the next section we will use a quantitative indicator of the sublattice polarization for studying the transition.

5.3 Sublattice Polarization and robustness of the edge states

5.3.1 Sublattice Polarization

Generally, the system's topology is described in the reciprocal space in the bulk system, whose consequences are observed in the edge. Nevertheless, recent studies have shown that real-space descriptors can characterize the topology of a system[64, 65, 66]. In particular, the sublattice polarization can characterize the topology of SSH-edge states, predicting the topological phase of the system regardless of bulk[66]. As we have seen previously, for
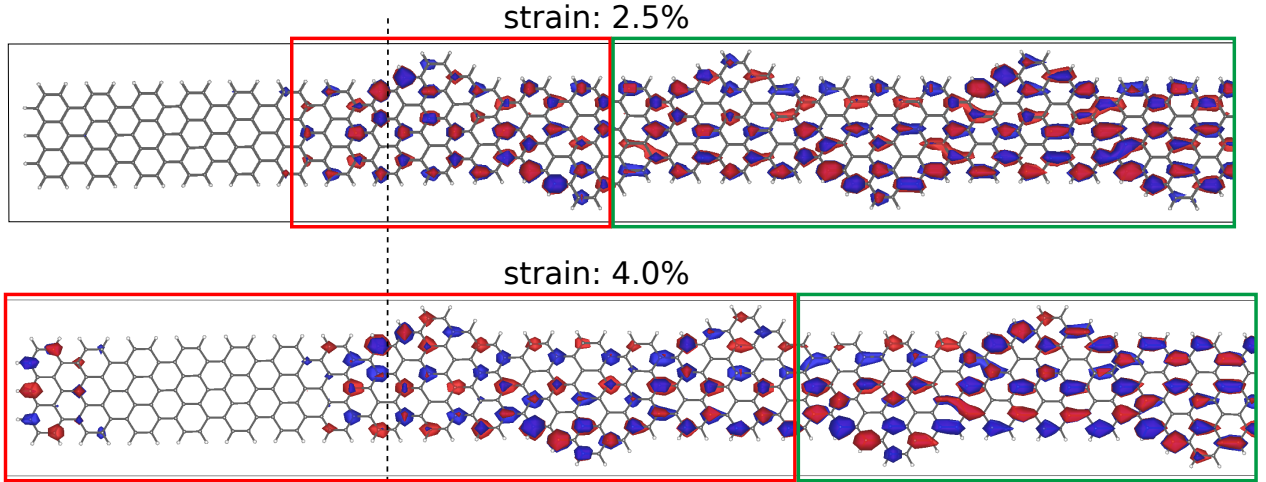
Figure 5.6: Topological transition of the 7-AGNR-$S(1,3)$ under strain. The wave function of one of the levels involved (black symbols in Fig. 5.5) is plotted. The regions of the band structure with/without an evident sublattice polarization (*i.e.* as in a topological state) are enclosed by a red/green frame.

low energies, AGNR superlattices under strain behave like an SSH system, giving us the possibility to describe the topological states by means of the sublattice polarization. Indeed, the electrical transport in AGNR superlattices can be described by the degree of sublattice polarization of its topological-like modes.[67] Before continuing, a few remarks about the sublattice polarization are needed. The definition of sublattice polarization, $|\psi_A|^2 - |\psi_B|^2$, has been employed before[68], but it can not be readily applied for a superlattice geometry. The hybridization of the sublattice polarized states (*e.g.* $|\phi_A^{left}\rangle \pm |\phi_B^{right}\rangle$) gives a zero net polarization, regardless of the nature of the states. The sublattice polarization is well preserved at a *local* scale but not along the whole superlattice. We define a number $P_{A/B}$, that gives an account of the sublattice polarization of the whole system at the *local* scale:

$$P_{A/B}^n = \frac{\sum_{i,j}\left(|\psi_i^{(n)}|^2 - |\psi_j^{(n)}|^2\right)}{\sum_{i,j}\left(|\psi_i^{(n)}|^2 + |\psi_j^{(n)}|^2\right)}, \tag{5.2}$$

where $\psi^{(n)}$ is the wave-function of the n-th energy level, the summation runs over all nearest-neighbor pairs, and N is the number of electrons. Locally, if the atom i belongs to one sublattice, its nearest neighbors must belong to the other sublattice. But, we are not explicitly labelling them. In a fully delocalized state without any sublattice polarization, $P_{A/B} = 0$. In a perfectly sublattice polarized state, $P_{A/B} = 1$, regardless of the localization. The outer absolute value in eqn. (5.2) is useful to avoid a net zero value of the indicator, likely to occur with two edges.
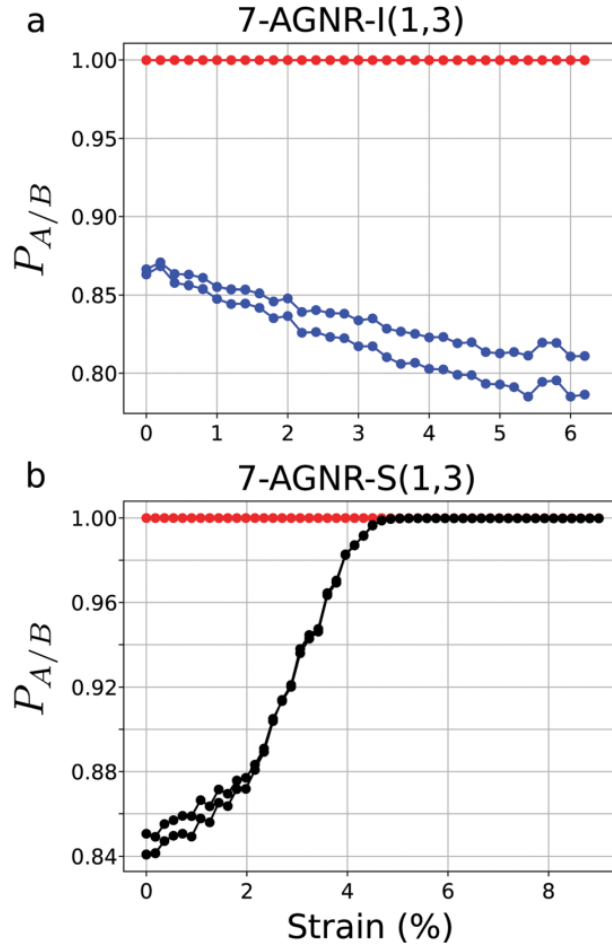
Figure 5.7: Sublattice polarization, as defined in eqn (49) for selected states of each superlattice. The states use the same color scheme as Fig. 5.5 In panel a the red curves are four topologically-protected states (i.e. there are four red lines), and two trivial bulk states in blue. In panel b there are two topological states (red lines), and two states involved in the topological transition (black lines)

5.3.2 Topological transition

Fig. 5.7 shows $P_{A/B}$ for some selected states of each superlattice. Conceptually, the case of 7-AGNR-I(1,3) is clear regardless of the strain, since the states colored blue (see Fig. 5.5a) correspond to non-topological SSH-like energy levels, and they have $P_{A/B} > 1$. Their value of $P_{A/B}$ is quite high, which is not unexpected since the building blocks for the SSH-like chain are sublattice-polarized states. Instead, the four topological states – colored red – have $P_{A/B} \approx 1$. regardless of the strain value. These topological states correspond to linear combinations of two zigzag edge states, plus two states at the edge of the super-lattice. Without the zigzag edges (*i.e* semi-infinite boundary conditions in the left and right leads), only the two edge states coming from the superlattice should appear, they should be hybridized in even and odd states, as it happens in regular SSH chains. ([42]).

A remarkable topological transition near 5.0% can be seen in the bottom panel of fig.5.5 for the 7-AGNR-S(1,3) case (black dots). Below the topological transition, $P_{A/B}$ increases

steadily with the strain, from its bulk value (at zero strain its value is close to the trivial state shown in Fig. 5.5, but near the transition its increase is very quick, suggesting the utility of thi index to characterize the process.

5.4 Methods

For calculating the mechanical properties of AGNRs, we used classical molecular dynamics (MD) simulations , applying uniaxial deformation to the AGNR. MD simulations were carried out with the LAMMPS software[69], using the REBO-scr potential.[70] It has been shown that this potential gives a reliable description of the strain-stress processes (including bond breaking) in AGNRs and other C-based systems[53, 59]. Studied superlattices have finite size and were thermalized at 10 K. We used long periodic superlattices, and homogeneous strain was applied, with a strain rate of 1×10^9 s^{-1}. Visualization was done with OVITO [71]. The finite 7-AGNR-I(1,3) consists of 10 unit cells of the supercell pattern (see Fig. 5.1), plus 7 unit cells of 7-AGNR backbone leads, a total of 750 C atoms. The finite 7- AGNR-I(1,3) consists of 8 unit cells of the supercell pattern (see Fig. 5.1), plus 7 unit cells of 7-AGNR backbone leads, a total of 978 C atoms. All samples are hydrogenated.

The electronic structure was calculated using some of the atomic configurations obtained by the MD simulations explained above. Given the large number of electrons in the superlattices, most of the calculations were carried out using density functional based tight-binding, as implemented in the DFTB+ package [56, 72]. Our calculations of the phonon spectrum of graphene with DFTB and DFT gave similar results. For the analysis of the electronic structure we used a modified version of PyProcar[73] that exploits the sublattice polarization of the topological states.

A commentary about the accuracy of our DFTB approach, and its influence on our results is needed. The band gaps of a freestanding N-AGNR calculated using simpler DFT functionals (LDA or PBE), DFTB, and simple tight-binding models are similar. Nevertheless, different levels of the theory give different results. The screened hybrid functional HSE06[74] gives band gaps $\Delta_7 \approx 2.1[eV]$ and $\Delta_9 \approx 1.2[eV]$ [75] According to GW calculations the quasiparticle band gaps are $\Delta_7 \approx 3.8[eV]$ and $\Delta_9 = 2.9[eV]$, respectively [76].

Regardless of the possible (large) inaccuracies in the band-gaps, the mechanism presented here for a strain-driven topological transition should remain valid, but it is not clear if it would require unrealistically large strain values. In the following lines we will argue that it is not the case.

It has been shown, by using a simple tight-binding model, that when applying a uniform strain, the band gap of an AGNR has a cyclic behavior, it increases until reaching a maximum, then it decreases until reaching a minimum and repeats (the equilibrium geometry can be anywhere within the cycle). This effect only depends on: (i) the deformation of the reciprocal space due to the strain, and (ii) the change in the position of the subbands with respect to the Dirac cone, hence it is not affected by the level of the theory employed. For reference, the strains needed to go from a maximum to a minimum are 17.5% for 7-AGNR and 13.5% for 9-AGNR. [44].

We will build a simple model to adjust the GW values of the band gaps (*i.e.*, the case with the largest differences). Assuming a linear dependence of the band gaps Δ_7, Δ_9 with the strain, the model needs two values of Δ_7 and Δ_9 at different strains. One set of data is the GW band gaps at zero strain. The others are the values of the strain at which Δ_7, Δ_9 have their minimum; as we mentioned before, these strains do not depend on the level of the theory employed. We calculate these strains to be 13% for 7-AGNR and 9% for 9-AGNR. It only remains to get the values of the (GW) band gap at these strain values, or $min(\Delta_7), min(\Delta_9)$. There is a formula to approximate the GW band gaps of freestanding unstrained AGNRs [76]:

$$\Delta_N = \frac{a}{w + w_0 + \delta},$$ (5.3)

where a and δ are parameters depending on the family of AGNR, w is the width in $\mathring{A}$ and $w_0 = 2.4\mathring{A}$ [76]. We will use the values $a = 14.6[eV]$ and $\delta = -0.4$. corresponding to a $N = 3p + 2$ ('metallic') AGNR. The minimum band gap of an AGNR under strain occurs when a subband passes by the exact location of a Dirac cone, the same situation of an unstrained $N = 3p + 2$ AGNR. This gives $min(\Delta_9) = 1.2[eV]$ and $min(\Delta_7) = 1.6[eV]$. With this data, we found $\Delta_7 = \Delta_9$ at a strain of $\approx 2.5\%$, even smaller than our earlier estimation from DFTB calculations.

Experimentally, the 7/9-AGNRs are synthesized on top of an Au(111) surface. The effect of the Au surface in the electronic structure of the GNR seems to be an increase of the screening. Accordingly, the quasi-particle effects are smaller than in freestanding GNRs, and the band gaps decrease. The experimental band gap of the 7-AGNR on Au(111) is between 2.3 and 2.7$[eV]$ [77, 78, 79] and it is 1.5$[eV]$ for 9-AGNR.[79] Even though these values are much smaller than the ones in freestanding AGNRs, they are still far from the LDA or tight binding values. Following the discussion for the freestanding case, the critical strain for achieving the topological transition in the 7-AGNR-$S(1,3)$ superlattice should not be too different from our results. This is based on the fact that the strains needed to have a minimum of the band gaps of 7-AGNR and 9-AGNR should be very close to the freestanding case (the additional strain due to the gold should be very small). In other words a larger or smaller band gap should be compensated by a faster or slower change of the band gap with the strain.

Chapter 6

Summary and Conclusions

We studied the electronic and mechanical properties under strain of superlattices formed by 7-AGNR and 9-AGNR. These AGNRs have a different geometrical phase, and the entire superlattice -at low energies- resembles the SSH model: a bipartite chain with nearest neighbors interactions t, t'. The SSH model has two topological phases: $t > t'$ and $t < t'$, and depending on the actual edges, one of phases has zero-energy topologically-protected edge states.

Our main contribution is to identify a mechanism to induce a topological transition by means of strain. Different topological classes of AGNR, such as 7-AGNR and 9-AGNR, have an opposite evolution of the band gap with strain. This implies an opposite evolution of the localization length of the boundary states, *i.e.* the states forming the SSH-like system. Therefore, the interactions t, t' have an opposite behavior with respect to strain. For the particular case of the superlattices formed by 7-AGNR and 9-AGNR, the interaction through the 7-AGNR increases with strain, but the interaction passing through the 9-AGNR decreases with strain. Depending on what interaction is larger without any strain, a topological transition should take place.

The topological states of the superlattice -if present and no topological transition takes place- are robust to strain even close to fracture. This is not surprising since strain does not break the chiral symmetry protecting the edge states. By means of the sublattice polarization, we were able to characterize the transition by means of the sublattice polarization of the system.

Classical molecular dynamics simulations show that mechanical properties change due to modulation, but staggered graphene nanoribbons have nearly the same fracture strain as unmodulated ribbons, therefore they support a large strain and this mechanism of topological transition should be valid for several other types of superlattices.

Recently, two specific GNR superlattices have been synthesized resembling massive[24] or even massless[67] Dirac fermions at the low-energy limit. Here, by using a moderate strain in 7-AGNR-S(1,3), we found a continuum of band gaps, including both the massless and massive Dirac fermion behaviors, close and just above the transition, respectively. The superlattice geometry of AGNR explored here opens a way to induce several exotic (mostly topological)

effects, which could have applications in electronics and quantum computing.

Bibliography

[1] E. Flores, J. D. Mella, E. Aparicio, R. Gonzalez, C. Parra, E. Bringa, and F. Munoz, "Inducing a topological transition in graphene nanoribbon superlattices by external strain," *Physical Chemistry Chemical Physics*, vol. 24, no. 11, pp. 7134–7143, 2022.

[2] O. Gröning, S. Wang, X. Yao, C. A. Pignedoli, G. B. Barin, C. Daniels, A. Cupo, V. Meunier, X. Feng, A. Narita, *et al.*, "Engineering of robust topological quantum phases in graphene nanoribbons," *Nature*, vol. 560, no. 7717, pp. 209–213, 2018.

[3] C. L. Kane and E. J. Mele, "Quantum spin hall effect in graphene," *Physical review letters*, vol. 95, no. 22, p. 226801, 2005.

[4] Y. Zhang, Y.-W. Tan, H. L. Stormer, and P. Kim, "Experimental observation of the quantum hall effect and berry's phase in graphene," *nature*, vol. 438, no. 7065, pp. 201–204, 2005.

[5] K. S. Novoselov, A. K. Geim, S. V. Morozov, D.-e. Jiang, Y. Zhang, S. V. Dubonos, I. V. Grigorieva, and A. A. Firsov, "Electric field effect in atomically thin carbon films," *science*, vol. 306, no. 5696, pp. 666–669, 2004.

[6] K. S. Novoselov, A. K. Geim, S. V. Morozov, D. Jiang, M. I. Katsnelson, I. Grigorieva, S. Dubonos, Firsov, and AA, "Two-dimensional gas of massless dirac fermions in graphene," *nature*, vol. 438, no. 7065, pp. 197–200, 2005.

[7] P. San-Jose, E. Prada, E. McCann, and H. Schomerus, "Pseudospin valve in bilayer graphene: towards graphene-based pseudospintronics," *Physical review letters*, vol. 102, no. 24, p. 247204, 2009.

[8] F. Xia, D. B. Farmer, Y.-m. Lin, and P. Avouris, "Graphene field-effect transistors with high on/off current ratio and large transport band gap at room temperature," *Nano Letters*, vol. 10, no. 2, pp. 715–718, 2010.

[9] F. Wang, Y. Zhang, C. Tian, C. Girit, A. Zettl, M. Crommie, and Y. R. Shen, "Gate-variable optical transitions in graphene," *science*, vol. 320, no. 5873, pp. 206–209, 2008.

[10] F. Xia, T. Mueller, Y.-m. Lin, A. Valdes-Garcia, and P. Avouris, "Ultrafast graphene photodetector," *Nature nanotechnology*, vol. 4, no. 12, pp. 839–843, 2009.

[11] L. P. Biró, P. Nemes-Incze, and P. Lambin, "Graphene: nanoscale processing and recent applications," *Nanoscale*, vol. 4, pp. 1824–1839, 2012.

[12] Y. Zhang, T.-T. Tang, C. Girit, Z. Hao, M. C. Martin, A. Zettl, M. F. Crommie, Y. R. Shen, and F. Wang, "Direct observation of a widely tunable bandgap in bilayer graphene," *Nature*, vol. 459, no. 7248, pp. 820–823, 2009.

[13] Z. H. Ni, T. Yu, Y. H. Lu, Y. Y. Wang, Y. P. Feng, and Z. X. Shen, "Uniaxial strain on graphene: Raman spectroscopy study and band-gap opening," *ACS nano*, vol. 2, no. 11, pp. 2301–2305, 2008.

[14] V. M. Pereira, A. C. Neto, and N. Peres, "Tight-binding approach to uniaxial strain in graphene," *Physical Review B*, vol. 80, no. 4, p. 045401, 2009.

[15] M. Sui, G. Chen, L. Ma, W.-Y. Shan, D. Tian, K. Watanabe, T. Taniguchi, X. Jin, W. Yao, D. Xiao, *et al.*, "Gate-tunable topological valley transport in bilayer graphene," *Nature Physics*, vol. 11, no. 12, pp. 1027–1031, 2015.

[16] L. Ju, Z. Shi, N. Nair, Y. Lv, C. Jin, J. Velasco, C. Ojeda-Aristizabal, H. A. Bechtel, M. C. Martin, A. Zettl, *et al.*, "Topological valley transport at bilayer graphene domain walls," *Nature*, vol. 520, no. 7549, pp. 650–655, 2015.

[17] F. Munoz, H. O. Collado, G. Usaj, J. O. Sofo, and C. Balseiro, "Bilayer graphene under pressure: Electron-hole symmetry breaking, valley hall effect, and landau levels," *Physical Review B*, vol. 93, no. 23, p. 235443, 2016.

[18] M. J. Park, S. Jeon, S. Lee, H. C. Park, and Y. Kim, "Higher-order topological corner state tunneling in twisted bilayer graphene," *Carbon*, vol. 174, pp. 260–265, 2021.

[19] D. A. Bahamon, G. Gómez-Santos, and T. Stauber, "Emergent magnetic texture in driven twisted bilayer graphene," *Nanoscale*, vol. 12, pp. 15383–15392, 2020.

[20] Y.-W. Son, M. L. Cohen, and S. G. Louie, "Energy gaps in graphene nanoribbons," *Physical review letters*, vol. 97, no. 21, p. 216803, 2006.

[21] P. H. Jacobse, A. Kimouche, T. Gebraad, M. Ervasti, J. Thijssen, P. Liljeroth, and I. Swart, "Electronic components embedded in a single graphene nanoribbon," *Nature communications*, vol. 8, no. 1, pp. 1–7, 2017.

[22] M. El Abbassi, M. L. Perrin, G. B. Barin, S. Sangtarash, J. Overbeck, O. Braun, C. J. Lambert, Q. Sun, T. Prechtl, A. Narita, *et al.*, "Controlled quantum dot formation in atomically engineered graphene nanoribbon field-effect transistors," *ACS nano*, vol. 14, no. 5, pp. 5754–5762, 2020.

[23] R. S. K. Houtsma, J. de la Rie, and M. Stöhr, "Atomically precise graphene nanoribbons: interplay of structural and electronic properties," *Chem. Soc. Rev.*, vol. 50, pp. 6541–6568, 2021.

[24] Q. Sun, O. Gröning, J. Overbeck, O. Braun, M. L. Perrin, G. Borin Barin, M. El Abbassi, K. Eimre, E. Ditler, C. Daniels, V. Meunier, C. A. Pignedoli, M. Calame, R. Fasel, and P. Ruffieux, "Massive dirac fermion behavior in a low bandgap graphene nanoribbon near a topological phase boundary," *Advanced Materials*, vol. 32, no. 12, p. 1906054, 2020.

[25] J. Lawrence, P. Brandimarte, A. Berdonces-Layunta, M. S. G. Mohammed, A. Grewal, C. C. Leon, D. Sánchez-Portal, and D. G. de Oteyza, "Probing the magnetism of topological end states in 5-armchair graphene nanoribbons," *ACS Nano*, vol. 14, no. 4, pp. 4499–4508, 2020.

[26] A. D. Zdetsis and E. Economou, "Topological metal-insulator transition in narrow graphene nanoribbons?," *Carbon*, vol. 176, pp. 548–557, 2021.

[27] X. Wang and H. Dai, "Etching and narrowing of graphene from the edges," *Nature Chemistry*, vol. 2, pp. 661–665, 2010.

[28] J. Bai, X. Duan, and Y. Huang, "Rational fabrication of graphene nanoribbons using a nanowire etch mask," *Nano Letters*, vol. 9, no. 5, pp. 2083–2087, 2009. PMID: 19344151.

[29] L. Jiao, X. Wang, G. Diankov, H. Wang, and H. Dai, "Facile synthesis of high-quality graphene nanoribbons," *Nature Nanotechnology*, vol. 5, pp. 321–325, 2010.

[30] M. Sprinkle, M. Ruan, Y. Hu, J. Hankinson, M. Rubio-Roy, B. Zhang, X. Wu, C. Berger, and W. de Heer, "Scalable templated growth of graphene nanoribbons on sic," *Nature Nanotechnology*, vol. 5, pp. 727–731, 2010.

[31] J. Cai, P. Ruffieux, R. Jaafar, M. Bieri, T. Braun, S. Blankenburg, M. Muoth, A. P. Seitsonen, M. Saleh, X. Feng, *et al.*, "Atomically precise bottom-up fabrication of graphene nanoribbons," *Nature*, vol. 466, no. 7305, pp. 470–473, 2010.

[32] R. Ortiz, N. A. García-Martínez, J. L. Lado, and J. Fernández-Rossier, "Electrical spin manipulation in graphene nanostructures," *Phys. Rev. B*, vol. 97, p. 195425, May 2018.

[33] Q. Sun, Y. Yan, X. Yao, K. Müllen, A. Narita, R. Fasel, and P. Ruffieux, "Evolution of the topological energy band in graphene nanoribbons," *The Journal of Physical Chemistry Letters*, vol. 12, no. 35, pp. 8679–8684, 2021. PMID: 34472868.

[34] D. J. Rizzo, G. Veber, T. Cao, C. Bronner, T. Chen, F. Zhao, H. Rodriguez, S. G. Louie, M. F. Crommie, and F. R. Fischer, "Topological band engineering of graphene nanoribbons," *Nature*, vol. 560, no. 7717, pp. 204–208, 2018.

[35] W. P. Su, J. R. Schrieffer, and A. J. Heeger, "Solitons in polyacetylene," *Phys. Rev. Lett.*, vol. 42, pp. 1698–1701, Jun 1979.

[36] T. Cao, F. Zhao, and S. G. Louie, "Topological phases in graphene nanoribbons: Junction states, spin centers, and quantum spin chains," *Phys. Rev. Lett.*, vol. 119, p. 076401, Aug 2017.

[37] Y.-L. Lee, F. Zhao, T. Cao, J. Ihm, and S. G. Louie, "Topological phases in cove-edged and chevron graphene nanoribbons: Geometric structures, z2 invariants, and junction states," *Nano Letters*, vol. 18, no. 11, pp. 7247–7253, 2018.

[38] K.-S. Lin and M.-Y. Chou, "Topological properties of gapped graphene nanoribbons with spatial symmetries," *Nano Letters*, vol. 18, no. 11, pp. 7254–7260, 2018.

[39] J. Jiang and S. G. Louie, "Topology classification using chiral symmetry and spin correlations in graphene nanoribbons," *Nano Letters*, vol. 21, no. 1, pp. 197–202, 2021.

[40] J.-W. Rhim, J. H. Bardarson, and R.-J. Slager, "Unified bulk-boundary correspondence for band insulators," *Phys. Rev. B*, vol. 97, p. 115143, Mar 2018.

[41] A. M. Pendás, J. Contreras-García, F. Pinilla, J. D. Mella, C. Cardenas, and F. Muñoz, "A chemical theory of topological insulators," *Chemical Communications*, vol. 55, no. 82, pp. 12281–12287, 2019.

[42] F. Munoz, F. Pinilla, J. Mella, and M. I. Molina, "Topological properties of a bipartite lattice of domain wall states," *Scientific reports*, vol. 8, no. 1, pp. 1–9, 2018.

[43] S.-M. Choi, S.-H. Jhi, and Y.-W. Son, "Effects of strain on electronic properties of graphene," *Phys. Rev. B*, vol. 81, p. 081407, Feb 2010.

[44] Y. Li, X. Jiang, Z. Liu, and Z. Liu, "Strain effects in graphene and graphene nanoribbons: the underlying mechanism," *Nano Research*, vol. 3, no. 8, pp. 545–556, 2010.

[45] L. Sun, Q. Li, H. Ren, H. Su, Q. W. Shi, and J. Yang, "Strain effect on electronic structures of graphene nanoribbons: A first-principles study," *The Journal of Chemical Physics*, vol. 129, no. 7, p. 074704, 2008.

[46] F. Zhao, T. Cao, and S. G. Louie, "Topological phases in graphene nanoribbons tuned by electric fields," *Phys. Rev. Lett.*, vol. 127, p. 166401, Oct 2021.

[47] W. Wang, X. Lü, and H. Xie, "Floquet bands and photon-induced topological edge states of graphene nanoribbons," *Chinese Physics B*, vol. 30, no. 6, p. 066701, 2021.

[48] J. K. Asbóth, L. Oroszlány, and A. Pályi, "A short course on topological insulators," *Lecture notes in physics*, vol. 919, p. 166, 2016.

[49] J. D. Mella, "Nuevos estados topológicos en heteroestructuras basadas en aisladores topológicos.," *Repositorio Academico de la Universidad de Chile*, 2019.

[50] J. Zak, "Berry's phase for energy bands in solids," *Phys. Rev. Lett.*, vol. 62, pp. 2747–2750, Jun 1989.

[51] E. McCann and M. Koshino, "The electronic properties of bilayer graphene," *Reports on Progress in Physics*, vol. 76, p. 056503, apr 2013.

[52] L. Foa Torres, S. Roche, and J.-C. Charlier, *Introduction to Graphene-Based Nanomaterials: From Electronic Structure to Quantum Transport*. 01 2014.

[53] E. Aparicio, E. Tangarife, F. Munoz, R. Gonzalez, F. Valencia, C. Careglio, and E. Bringa, "Simulated mechanical properties of finite-size graphene nanoribbons," *Nanotechnology*, vol. 32, no. 4, p. 045709, 2020.

[54] M. Oliva Leyva, "Hamiltoniano efectivo de dirac para el grafeno deformado : propiedades electrónicas y ópticas". (tesis de doctorado).," *Universidad Nacional Autónoma de México*, 2016.

[55] Y. Chu, T. Ragab, and C. Basaran, "The size effect in mechanical properties of finite-sized graphene nanoribbon," *Computational Materials Science*, vol. 81, pp. 269–274, 2014.

[56] B. Hourahine, B. Aradi, V. Blum, F. Bonafé, A. Buccheri, C. Camacho, C. Cevallos, M. Deshaye, T. Dumitrică, A. Dominguez, *et al.*, "Dftb+, a software package for efficient approximate density functional theory based atomistic simulations," *The Journal of chemical physics*, vol. 152, no. 12, p. 124101, 2020.

[57] S. Datta, *Quantum transport: atom to transistor.* Cambridge university press, 2005.

[58] Y. Gao, W. Yang, and B. Xu, "Unusual thermal conductivity behavior of serpentine graphene nanoribbons under tensile strain," *Carbon*, vol. 96, pp. 513–521, 2016.

[59] E. Tangarife, R. Gonzalez, C. Cardenas, E. Bringa, and F. Munoz, "Molecular simulations of carbon allotropes in processes with creation and destruction of chemical bonds," *Carbon*, vol. 144, pp. 177–184, 2019.

[60] K. Suzuki, R. Nakagawa, Q. Zhang, and H. Miura, "Development of highly sensitive strain sensor using area-arrayed graphene nanoribbons," *Nanomaterials*, vol. 11, p. 1701, Jun 2021.

[61] A. Taqieddin and N. R. Aluru, "Electronic structure and transport in graphene nanoribbon heterojunctions under uniaxial strain: Implications for flexible electronics," *ACS Applied Nano Materials*, vol. 4, no. 6, pp. 5816–5824, 2021.

[62] G. Kliros, "Strain effects on the quantum capacitance of graphene nanoribbon devices," *Applied Surface Science*, vol. 502, p. 144292, 02 2020.

[63] E. Louis, E. San-Fabián, G. Chiappe, and J. A. Vergés, "Electron enrichment of zigzag edges in armchair–oriented graphene nano–ribbons increases their stability and induces pinning of the fermi level," *Carbon*, vol. 154, pp. 211–218, 2019.

[64] H. Huang and F. Liu, "Quantum spin hall effect and spin bott index in a quasicrystal lattice," *Phys. Rev. Lett.*, vol. 121, p. 126401, Sep 2018.

[65] X. S. Wang, A. Brataas, and R. E. Troncoso, "Bosonic bott index and disorder-induced topological transitions of magnons," *Phys. Rev. Lett.*, vol. 125, p. 217202, Nov 2020.

[66] A. Martín Pendás, F. Muñoz, C. Cardenas, and J. Contreras-García, "Understanding topological insulators in real space," *Molecules*, vol. 26, no. 10, p. 2965, 2021.

[67] D. J. Rizzo, G. Veber, J. Jiang, R. McCurdy, T. Cao, C. Bronner, T. Chen, S. G. Louie, F. R. Fischer, and M. F. Crommie, "Inducing metallicity in graphene nanoribbons via zero-mode superlattices," *Science*, vol. 369, no. 6511, pp. 1597–1603, 2020.

[68] A. L. Pereira and P. Schulz, "Valley polarization effects on localization in graphene landau levels," *Physical Review B*, vol. 77, no. 7, p. 075416, 2008.

[69] S. Plimpton, "Fast parallel algorithms for short-range molecular dynamics," *Journal of Computational Physics*, vol. 117, no. 1, pp. 1 – 19, 1995.

[70] L. Pastewka, P. Pou, R. Pérez, P. Gumbsch, and M. Moseler, "Describing bond-breaking processes by reactive potentials: Importance of an environment-dependent interaction range," *Phys. Rev. B*, vol. 78, p. 161402, 2008.

[71] A. Stukowski, "Visualization and analysis of atomistic simulation data with ovito–the open visualization tool," *Modelling and Simulation in Materials Science and Engineering*, vol. 18, no. 1, p. 015012, 2009.

[72] M. Elstner, D. Porezag, G. Jungnickel, J. Elsner, M. Haugk, T. Frauenheim, S. Suhai, and G. Seifert, "Self-consistent-charge density-functional tight-binding method for simulations of complex materials properties," *Phys. Rev. B*, vol. 58, pp. 7260–7268, Sep 1998.

[73] U. Herath, P. Tavadze, X. He, E. Bousquet, S. Singh, F. Muñoz, and A. H. Romero, "Pyprocar: A python library for electronic structure pre/post-processing," *Computer Physics Communications*, vol. 251, p. 107080, 2020.

[74] J. Heyd, G. E. Scuseria, and M. Ernzerhof, "Hybrid functionals based on a screened coulomb potential," *The Journal of Chemical Physics*, vol. 118, no. 18, pp. 8207–8215, 2003.

[75] V. Barone, O. Hod, and G. E. Scuseria, "Electronic structure and stability of semiconducting graphene nanoribbons," *Nano Letters*, vol. 6, no. 12, pp. 2748–2754, 2006. PMID: 17163699.

[76] L. Yang, C.-H. Park, Y.-W. Son, M. L. Cohen, and S. G. Louie, "Quasiparticle energies and band gaps in graphene nanoribbons," *Phys. Rev. Lett.*, vol. 99, p. 186801, Nov 2007.

[77] P. Ruffieux, J. Cai, N. C. Plumb, L. Patthey, D. Prezzi, A. Ferretti, E. Molinari, X. Feng, K. Müllen, C. A. Pignedoli, and R. Fasel, "Electronic structure of atomically precise graphene nanoribbons," *ACS Nano*, vol. 6, no. 8, pp. 6930–6935, 2012. PMID: 22853456.

[78] H. Söde, L. Talirz, O. Gröning, C. A. Pignedoli, R. Berger, X. Feng, K. Müllen, R. Fasel, and P. Ruffieux, "Electronic band dispersion of graphene nanoribbons via fourier-transformed scanning tunneling spectroscopy," *Phys. Rev. B*, vol. 91, p. 045429, Jan 2015.

[79] O. Deniz, C. Sánchez-Sánchez, T. Dumslaff, X. Feng, A. Narita, K. Müllen, N. Kharche, V. Meunier, R. Fasel, and P. Ruffieux, "Revealing the electronic structure of silicon intercalated armchair graphene nanoribbons by scanning tunneling spectroscopy," *Nano Letters*, vol. 17, no. 4, pp. 2197–2203, 2017. PMID: 28301723.

[80] C. Outeiral, M. A. Vincent, Á. M. Pendás, and P. L. Popelier, "Revitalizing the concept of bond order through delocalization measures in real space," *Chemical science*, vol. 9, no. 25, pp. 5517–5529, 2018.

[81] M. Elstner, D. Porezag, G. Jungnickel, J. Elsner, M. Haugk, T. Frauenheim, S. Suhai, and G. Seifert, "Self-consistent-charge density-functional tight-binding method for simulations of complex materials properties," *Phys. Rev. B*, vol. 58, pp. 7260–7268, Sep 1998.

[82] G. Kresse and J. Hafner, "Ab initio molecular dynamics for liquid metals," *Phys. Rev. B*, vol. 47, pp. 558–561, 1993.

[83] G. Kresse and J. Hafner, "Ab initio molecular-dynamics simulation of the liquid-metal–amorphous-semiconductor transition in germanium," *Phys. Rev. B*, vol. 49, pp. 14251–14269, May 1994.

[84] G. Kresse and J. Furthmüller, "Efficiency of ab-initio total energy calculations for metals and semiconductors using a plane-wave basis set," *Comput. Mater. Sci.*, vol. 6, no. 1, pp. 15 – 50, 1996.

[85] G. Kresse and D. Joubert, "From ultrasoft pseudopotentials to the projector augmented-wave method," *Phys. Rev. B*, vol. 59, pp. 1758–1775, Jan 1999.

[86] J. P. Perdew, K. Burke, and M. Ernzerhof, "Generalized gradient approximation made simple," *Phys. Rev. Lett.*, vol. 77, pp. 3865–3868, 1996.

[87] "The proportionality factor can be different for different N-AGNR, but we will ignore it during the discussion, the most important part is its dependency with the band gap: The localization length decreases (increases) as the band gap increases (decreases)."

[88] Q. Sun, Y. Yan, X. Yao, K. Müllen, A. Narita, R. Fasel, and P. Ruffieux, "Evolution of the topological energy band in graphene nanoribbons," *The Journal of Physical Chemistry Letters*, vol. 12, no. 35, pp. 8679–8684, 2021.

[89] M. Fujita, K. Wakabayashi, K. Nakada, and K. Kusakabe, "Peculiar localized state at zigzag graphite edge," *Journal of the Physical Society of Japan*, vol. 65, no. 7, pp. 1920–1923, 1996.

Chapter 7

Annexes

Annex A

Supplementary information

A.1   Graphene Density of states

In condensed matter the Density Of States (DOS) are useful to determine the electronic and magnetic properties of a material. Experimentally DOS is measured through the change of the current generated by the energy of the electrons in the material sample, that is, through dI/dV.

For example, lower DOS for certain energy level means that few states can be occupied.
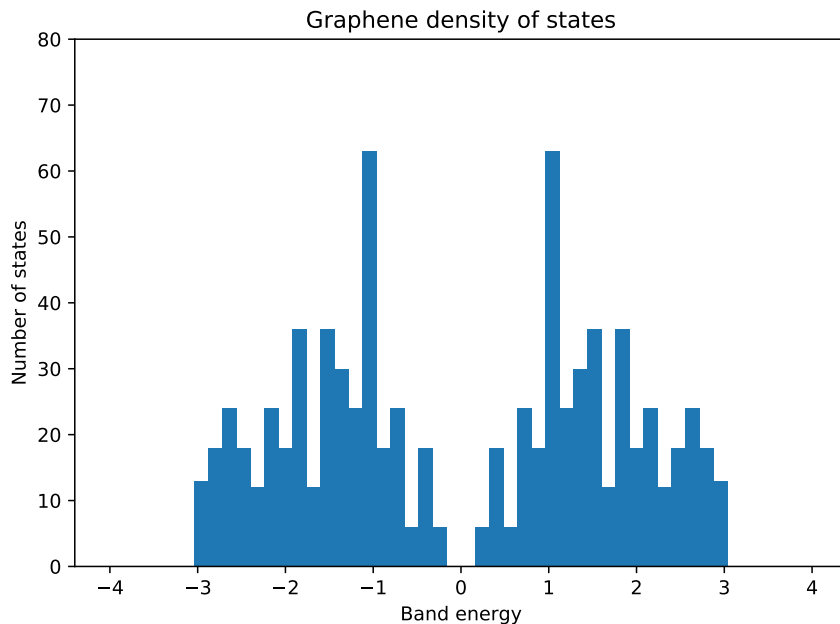

Figure A.1: Density of states of graphene, centered with respect to the fermi energy.

Annex B

Supplementary information

B.1 Experimental results

Although this thesis has a theoretical approach developed through simulations, Rizzo *et.al* [34] obtained these joints via bottom-up synthesis on Au(111). To do this it is necessary to create a molecular precursors to joint both different nanostructures and finally create a superlattice of these junctions.

Using the experimental technique of Scanning Tunneling Spectroscopy (STS) [34, 2], the topology of the system can be identified. The idea is to obtain the local density of states in the end of a segment and visualize the existence of zero energy localized states. To prevent the zero energy states of the zig-zag termination from interacting with the localized states of each termination, Gronig *et.al.* suggest doing an extension as shown by Figure B.1 (a).
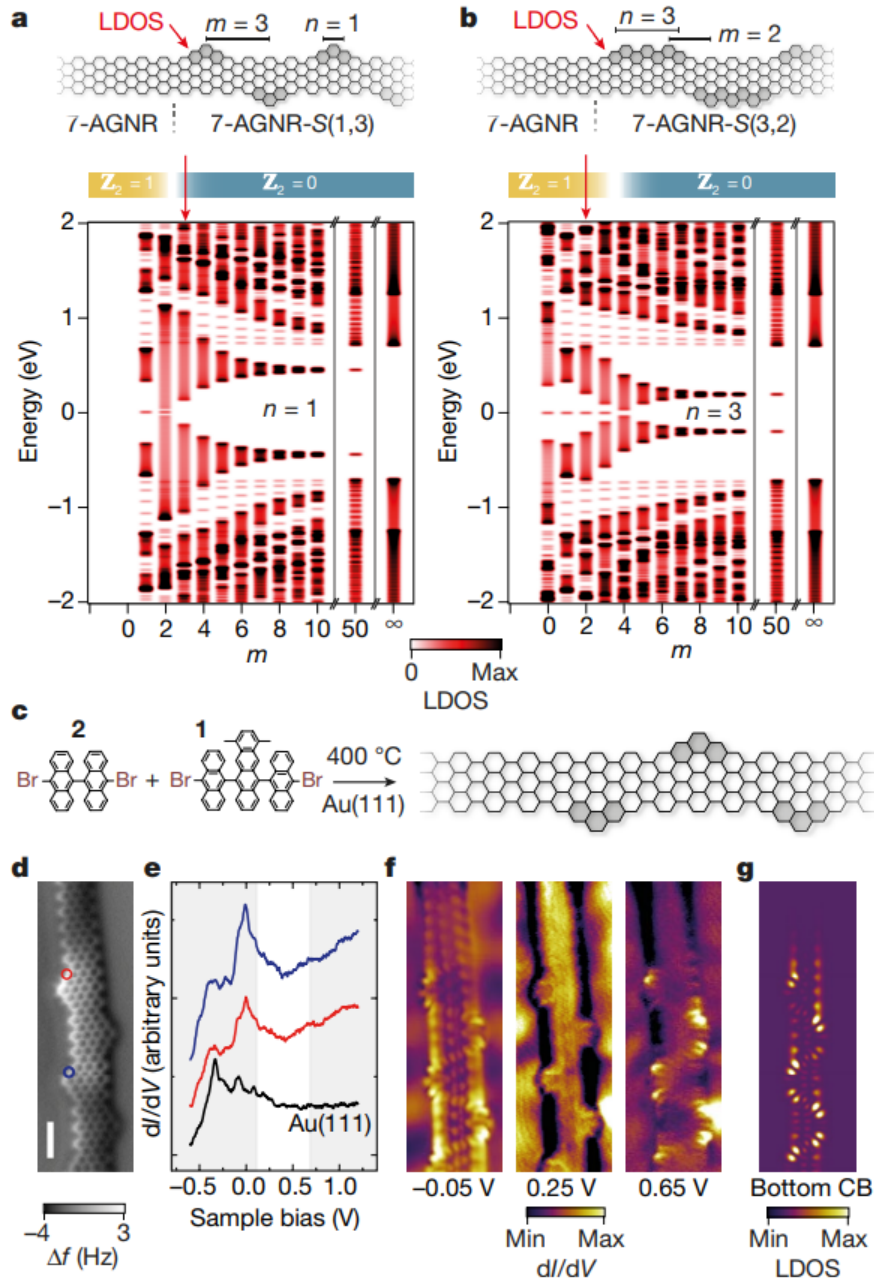
Figure B.1: This Figure was obtained in [2], see this reference for more details. Local density of states (LDOS) for the (a) $7-AGNR-S(1, m)$ and (b) $7-AGNR-S(3, m)$ evaluated at the end of the segment (see the row) as a function of the inter-segment spacing m. For example, the model in (a), the case of $7-AGNR-S(1,3)$ is topologically trivial, because there are no zero energy states. But in the case exposed in the upper part of (b), $7-AGNR-S(3,2)$ the existence of states of zero energy can be seen, therefore this case is of non-trivial topology. (c) Pathway to the $7-AGNR$ backbone extended $7-AGNR-S(1,3)$ nanoribbon using 1 and 2 as precursor molecules. (d) Constant-height nc-AFM frequency shift (Δf) image of a $7-AGNR-S(1,3)$ segment. (e) STS spectra taken at positions indicated by the markers of the corresponding colour in (d). (f) Experimental constant current dI/dV maps at the top of the valence band, in the gap and at the bottom of the conduction band. (g) Tight-binding-simulated charge-density map of the bottom of the conduction band, computed for the experimental results.
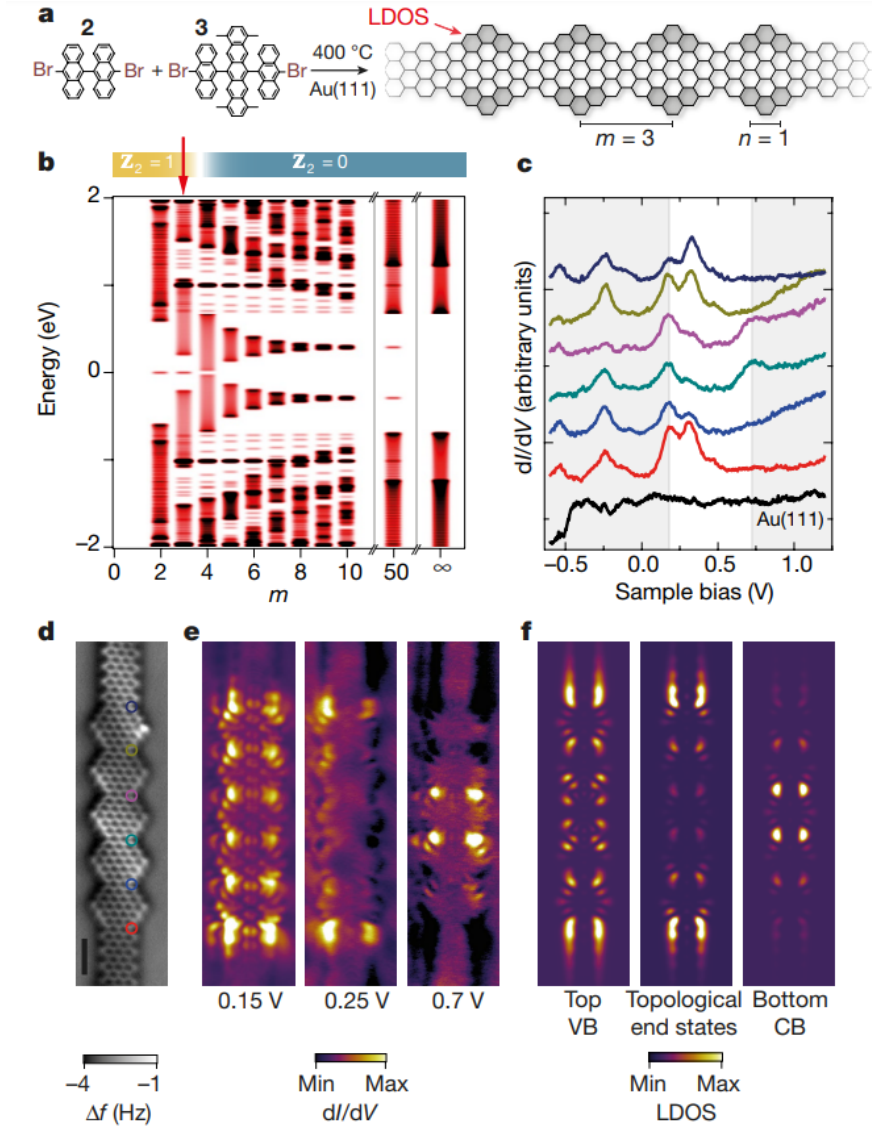
Figure B.2: This Figure was obtained in [2], see this reference for more details. (a) route to the 7-AGNR backbone extended 7-AGNR-S(1,3) nanoribbon using 2 and 3. (b) LDOS of $7 - AGNR - I(1,3)$ at the end of the segment plotted as a function of inter-segment spacing m. (c) dI/dV spectra at the locations indicated by the markers of corresponding colour in (d). In (d), Constant-height nc-AFM frequency shift (Δf) image of a 5-unit $7 - AGNR - I(1,3)$ segment with $7 - AGNR$ extensions at both ends. (e) Experimental dI/dV maps of the main spectroscopic features at different voltages. Tight-binding simulated charge-density maps at the top of the valence band, at $E = 0$ and at the bottom of conduction bands.

Annex C

Supplementary information

C.1 Fracture Process

In order to better understand the modulated AGNR fracture process, we include some MD snapshots in Figures C.1 and C.2. MD results were obtained out in collaboration with E. Aparicio.
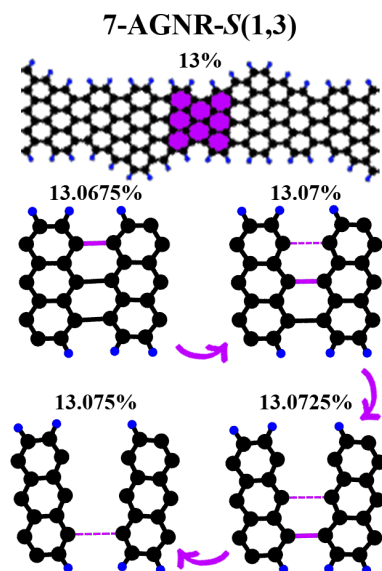

Figure C.1: 7-AGNR-S(1,3) superlattice at 13% strain when no bond has broken yet. Carbon atoms in black and hydrogen atoms in blue. The purple region marks the zone that will be involved in the fracture process. Detailed evolution of bond breaking in that purple region is presented as a function of strain, where purple thick bonds will break in the next snapshot and will be represented by dashed thin purple bonds.

7-AGNR-*I*(1,3)

Figure C.2: 7-AGNR-*I*(1,3) superlattice at 6.6% strain when no bond has broken yet. Carbon atoms in black and hydrogen atoms in blue. The purple region marks the zone that will be involved in the fracture process. Detailed evolution of bond breaking in that purple region is presented as a function of strain, where purple thick bonds will break in the next snapshot and will be represented by dashed thin purple bonds.
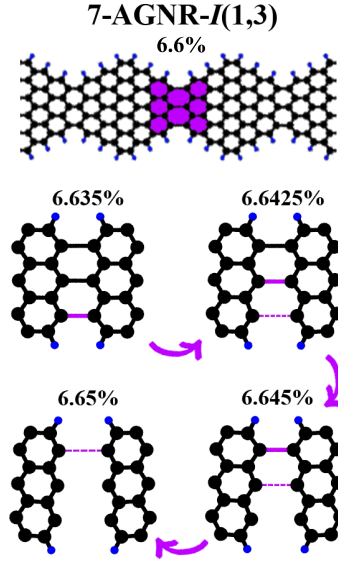
C.2 Penetration length of a zig-zag GNR

An exact expression for the edges states in zigzag terminated graphene (i.e. periodic along the y-axis) was found by Fujita *et.al.* [89]:

$$\psi_m \propto \cos^{2m}\left(\frac{k}{2}\right) \tag{C.1}$$

where m is the index of the site since the border, and k is wavevector from the periodic direction. The penetration length, ε is:

$$\varepsilon^{-1} = \ln\left[\cos^2\left(\frac{k}{2}\right)\right] \tag{C.2}$$

If we are interested in edge states with $E \approx 0$, the values of k of interest are close to π, or $k = \pi - \delta_y$. After some algebra, we find:

$$\frac{1}{\varepsilon} \approx \delta_y \tag{C.3}$$

Our case of interest is the penetration of the states from zigzag edges in an AGNR, not graphene. This imposes a quantization of the values of k allowed, and also gives rise to a band gap, then $\frac{1}{\varepsilon} \approx \frac{\Delta}{2t}$ with Δ the bandgap.